
This is an electronic reprint of the original article.
This reprint may differ from the original in pagination and typographic detail.

Karimkashi Arani, Shervin; Kaario, Ossi; Vuorinen, Ville

Effects of hydrogen enrichment and turbulence intensity on the combustion mode in locally stratified dual-fuel mixtures of n-dodecane/methane

Published in:
Applications in Energy and Combustion Science

DOI:
[10.1016/j.jaecs.2022.100072](https://doi.org/10.1016/j.jaecs.2022.100072)

Published: 01/06/2022

Document Version
Publisher's PDF, also known as Version of record

Published under the following license:
CC BY-NC-ND

Please cite the original version:
Karimkashi Arani, S., Kaario, O., & Vuorinen, V. (2022). Effects of hydrogen enrichment and turbulence intensity on the combustion mode in locally stratified dual-fuel mixtures of n-dodecane/methane. *Applications in Energy and Combustion Science*, 10, Article 100072. <https://doi.org/10.1016/j.jaecs.2022.100072>

This material is protected by copyright and other intellectual property rights, and duplication or sale of all or part of any of the repository collections is not permitted, except that material may be duplicated by you for your research use or educational purposes in electronic or print form. You must obtain permission for any other use. Electronic or print copies may not be offered, whether for sale or otherwise to anyone who is not an authorised user.



Effects of hydrogen enrichment and turbulence intensity on the combustion mode in locally stratified dual-fuel mixtures of n-dodecane/methane

Shervin Karimkashi*, Ossi Kaario, Ville Vuorinen

Aalto University, Department of Mechanical Engineering, School of Engineering, Otakaari 4, 02150 Espoo, Finland

ARTICLE INFO

Keywords:

Combustion mode
Dual-fuel
Diesel
Hydrogen
Methane

ABSTRACT

In dual-fuel (DF) engines, a high-reactivity fuel (HRF) ignites a low-reactivity fuel (LRF) premixed with air. Identification of the combustion mode after autoignition in DF engines with different fuel combinations and under various mixture stratification levels is of crucial importance since the combustion mode may affect the engine performance and emissions levels. However, to avoid expensive computational or experimental tests for different fuel combinations under various initial conditions, an analytical diagnostics tool can help identify the modes of combustion. Recently, we developed an a-priori tool (β -curve), which separates between the deflagration and spontaneous combustion modes in transient problems based on two parameters: HRF stratification amplitude and wavelength. However, the developed analysis was only evaluated for a single fuel combination and under 2D turbulent conditions. The present study extends our previous work by (1) evaluating the 1D β -curve analysis for more common fuel combinations including hydrogen, and (2) extending the combustion mode analysis to 3D turbulent combustion. First, using 1D numerical simulations, the combustion mode for a new DF combination of n-dodecane (HRF) and methane (LRF) with and without hydrogen enrichment in the LRF blend is investigated. Although hydrogen enrichment shortens the combustion duration, its role in changing the combustion mode remains subtle. Therefore, only n-dodecane/methane (no hydrogen enrichment) is considered in the 3D simulations to avoid highly expensive 3D numerical simulations with hydrogen enrichment. Second, using flame-resolved 3D numerical simulations, variations of the combustion mode for DF n-dodecane/methane mixtures at three different turbulence intensities are studied. It is observed that high turbulence levels can switch the combustion mode from deflagration to autoignition. For the first time, the diagnostic tool is evaluated compared to 3D turbulent numerical simulations and a correction factor is proposed in the β -curve equation.

1. Introduction

In heavy-duty dual-fuel (DF) engines operating under reactivity controlled compression ignition (RCCI) mode [1], a small amount of a high reactivity fuel (HRF) is utilized to ignite a low reactivity fuel (LRF) premixed with air. In such a scenario, different engine parameters such as compression ratio, injection parameters and air-throttling can affect the engine performance and emissions [2,3]. These different engine parameters may cause various levels of locally stratified HRF/LRF mixtures before ignition, which may lead to two common combustion modes: (i) subsonic spontaneous with autoignition fronts or (ii) deflagration [4]. The combustion mode has a significant impact on the targeted engine performance, including fuel consumption, emissions, and combustion duration [5]. Therefore, it is important to determine the prevalence of autoignition and deflagration fronts in stratified DF mixtures. In particular, where using different fuel combinations,

and specifically utilization of hydrogen blended with other fuels like methane, is growing rapidly, information on the combustion mode at different local stratification and turbulence levels is essential.

There are several works that investigate propagation modeling and physics of deflagration versus spontaneous ignition fronts. For instance, recently, autoignition of the end gas by premixed flame fronts in spark assisted homogeneous charge compression ignition engines was studied numerically by Zhang et al. [6]. Moreover, Savard et al. studied regimes of spontaneous versus deflagration under gas-turbine reheat combustion conditions [7]. In a following work, they investigated cool flames propagating in autoignitive mixtures to distinguish between deflagration and autoignition considering the relative importance of diffusion [8]. Stratified premixed flames have been also extensively studied in experiments [9–14] and numerical simulations [15–21], with a detailed overview given by Lipatnikov [22]. Different parameters are

* Corresponding author.

E-mail address: shervin.karimkashiarani@aalto.fi (S. Karimkashi).

studied in stratified flames. For instance, recently, Tomidokoro et al. studied the propagation speed of methane/hydrogen/air flames [23] and ammonia/air flames [24] in compositionally stratified mixtures under rich to lean and lean to rich conditions. Moreover, many studies have investigated effects of temperature [25–38] and/or composition [32–34,38,39] and/or velocity fluctuations [26,30,34,35,37] on the combustion mode for single-fuel conditions.

In the DF context, there are several studies on ignition characteristics [40–46], while direct numerical simulations (DNS) [47–51], numerical modeling [52–56], and experiments [57,58] have provided evidence on flame initiation after ignition, with detailed overview given by Li et al. [5]. Despite the abundance of studies on (1) characteristics of stratified premixed flames, (2) distinguishing between deflagration and spontaneous combustion under various conditions, and (3) numerical modeling or experimental studies on DF engines with various fuel combinations, the literature is scarce on providing an analytical tool which can give regime diagrams on the mode of combustion in a range of different stratification and turbulence levels in DF mixtures. This information is essential when changing fuel combinations and/or initial conditions may lead to different combustion modes. While we developed an analytical tool to distinguish between deflagration and spontaneous ignition in our recent work [59], the tool still requires further validations and improvements to be broadly used by the community.

This study attempts to improve the validation of the analytical tool in our previous work, which was limited to a single fuel combination and 2D turbulent conditions. In our recent paper [59], the deflagration and spontaneous combustion modes in DF mixtures were characterized based on the initial stratification of the HRF and LRF, under engine-like conditions, by extension of the Zeldovich theory [4] to transient conditions. The combustion modes were separated by two main parameters: amplitude and wavelength of the HRF stratification. An analytical a-priori diagnostics tool for the time-dependent diffusion–reaction problem, called β -curve, was developed by solving the diffusion equation while taking ignition and flame propagation time-scales into account. For turbulent conditions, enhanced mixing due to convection was incorporated via an effective mass diffusivity estimated based on the turbulence length-scale and velocity [60,61]. The developed model in Ref. [59] was first validated under laminar conditions for different stratification levels of the considered HRF (*n*-dodecane) and LRF (methanol) premixed with air using one-dimensional (1D) chemical kinetics numerical simulations. Second, the model was validated under turbulent conditions using fully-resolved two-dimensional (2D) turbulent numerical simulations. In the present work, first, we re-validate the developed model for *n*-dodecane/methane DF mixtures, where *n*-dodecane is the HRF and methane is the LRF, using 1D simulations. More importantly, effects of hydrogen enrichment on the combustion mode in 1D are discussed. Second, in contrast to the utilized 2D flows in our previous work, turbulence intensity effects on the combustion mode is studied by three-dimensional (3D) numerical simulations and the validity of the diagnostic tool is evaluated. We note that in this work, hydrogen enrichment effects are studied only under 1D laminar conditions to limit the 3D computational costs. In the following, a summary of the importance of including hydrogen in the LRF mixture and the relevance of using 3D turbulence in the numerical simulations is provided.

In the DF engines context, utilization of diesel (or its surrogates) as the HRF with natural gas or methane (CH₄) as the LRF has been already tested and established [62–65]. On the other hand, hydrogen is a highly attractive carbon-free alternative fuel in modern combustion systems, which is helpful in decarbonizing the combustion systems [66–68]. Various recent studies have demonstrated the benefits of hydrogen enrichment of the LRF in the RCCI context [69–74]. Blending methane (as the LRF) with hydrogen while using *n*-dodecane as the diesel surrogate was recently investigated in Ref. [75] using zero-dimensional (0D) homogeneous reactor simulations along with a reaction sensitivity

analysis. This work was recently extended to 3D spray simulations in Refs. [71,72]. Based on the numerical findings by Karimkashi et al. [75] and Kannan et al. [71], blending hydrogen with methane as the LRF delays the ignition timing, which can facilitate robust ignition. However, it was shown that ignition delay time (IDT) retardation is significant only when more than 50% volumetric hydrogen is added to methane at lean conditions (equivalence ratio of 0.5). Moreover, according to the literature [69,70], blending methane (LRF) with hydrogen reduces fuel consumption per cycle, shortens the combustion duration (improving the combustion process), and mitigates carbon emissions in RCCI engines. Accordingly, in this work, the impact of adding hydrogen to methane on the combustion mode is explored for *n*-dodecane/methane DF mixtures under laminar conditions (1D).

Turbulence intensity can enhance mixing before ignition and promote the spontaneous mode in stratified DF mixtures. However, turbulent simulations in our previous work [59] were 2D, which may lead to unrealistic features such as inverse energy cascade. For instance, 2D turbulence structure dynamics and their interactions with flow and thermal fields in engine-relevant conditions are discussed in Refs. [76–78]. Apart from 2D limitations in our previous work, a systematic control of the initial turbulence length-scale and velocity with the initialized Taylor–Green Vortex flows was challenging. In this study, 3D numerical simulations in cubic domains with decaying isotropic homogeneous turbulence are considered. The initial field is generated with an initial turbulent kinetic energy spectrum function by Passot–Pouquet [79]. Here, the initial turbulence intensity is systematically varied to explore effects of turbulence on the combustion mode. Subsequently, validity of the theory is re-evaluated.

In the present study, we apply the proposed analytical tool in Ref. [59] to different fuel combinations and we consider the effect of hydrogen enrichment in the LRF since hydrogen is of high importance to decarbonize combustion systems. Moreover, we utilize 3D numerical simulations for the validation of the analytical tool for the first time. The main feature of the 3D numerical simulations in this study is that a large and detailed chemical mechanism (which is essential when there is a combination of two or three fuels including a large hydrocarbon) is utilized under engine relevant conditions (high pressure and temperature) with low to high turbulence velocities. These 3D numerical simulations provide detailed information on the local structure of the ignition front in DF mixtures, which is not typically possible to be extracted in computationally demanding spray or engine simulations. The main objectives of the current work are to (1) extend the previous results on *n*-dodecane/methanol mixtures to *n*-dodecane/methane mixtures with and without hydrogen, (2) study the role of hydrogen enrichment on the combustion mode in 1D, (3) study effects of turbulence intensity on the combustion mode in *n*-dodecane/methane mixtures using flame-resolved 3D numerical simulations, (4) carry out an in-depth analysis on the combustion modes based on the 3D data for DF combustion, and (5) re-iterate the previously proposed β -curve theory using the 3D turbulent flame-resolved numerical simulations.

The paper is structured as follows. In the following section, first, the initial conditions for three different base mixtures of *n*-dodecane/methane with and without hydrogen enrichment are defined. Second, the initialization functions for the stratified mixtures in 1D and 3D are introduced. Then, the numerical solver is introduced and finally, a short summary of the β -curve theory is provided. The results are provided in two parts. In the first part, laminar 1D cases are introduced and their numerical simulation results as compared to the β -curve predictions are provided. In the second part, turbulent 3D cases are defined and the results are analyzed and different modes of combustion under different turbulence levels are identified. Finally, based on the 3D results, a correction factor is suggested in the theory. The paper concludes with final remarks and suggestions for future works.

Table 1

Initial conditions of the three defined mixture blends. The HRF is always *n*-dodecane and the LRF blending ratio (x) is reported ($\phi_{LRF} = 0.5$). Transient 1D simulations have initial mixtures fluctuating around these reported mass fractions.

x	T_{init} (K)	Y_{ndd}^{ave}	$Y_{CH_4}^{ave}$	$Y_{H_2}^{ave}$	$Y_{O_2}^{ave}$	$Y_{N_2}^{ave}$	
DF-x0	0	821	0.024	0.0277	0	0.221	0.7273
DF-x0.8	0.8	809.5	0.038	0.0138	0.0069	0.2193	0.722
DF-x1	1	804	0.05	0	0.0138	0.2182	0.718

2. Initial conditions and methodology

2.1. Initial conditions in 1D and 3D

In this follow-up work, *n*-dodecane (abbreviated as *ndd*), which is a diesel fuel surrogate, is kept as the HRF. However, the LRF is changed from methanol in Ref. [59] to different blends of methane/hydrogen, for which the LRF molar ratio is defined as $x = \frac{X_{H_2}}{X_{H_2} + X_{H_4}}$. Here, $x = 0, 0.8, \text{ and } 1$ are considered as the LRF blends, which are respectively denoted as DF-x0, DF-x0.8, and DF-x1. The considered x values are justified by the observations in Refs. [71,75], where adding $\approx 80\%$ volumetric hydrogen to methane leads to a significant change of τ_2 . The equivalence ratio of the LRF mixture premixed with air is considered as $\phi_{LRF} = 0.5$ in all the LRF blends. To set up 1D and 3D cases, first, the initial mixture conditions are selected following the procedure explained below. Second, the stratified mixtures are initiated as described in Section 2.2.

To define the initial mixture composition and temperature of the blends, a procedure similar to that in Ref. [59] is considered. First, using the 0D homogeneous reactor model in Cantera, the second-stage IDT versus mixture fraction profiles are plotted according to the mixing line concept [80]. In this study, the second-stage IDT (τ_2) is defined as the time instance when the maximum temperature of the domain reaches 1500 K. The initial pressure of the HRF and LRF streams is $p = 60$ bar while the initial temperature is $T = 363$ K for the HRF stream and 900 K for the LRF stream and $\phi_{LRF} = 0.5$. The selected values for pressure and temperature are relevant to those of the ECN spray A conditions [81], which are also considered in DF spray studies by several researchers at a similar ϕ_{LRF} , e.g. see [41,42,45,71,72,82]. Second, for each blend, the most reactive mixture fraction is identified and its initial temperature (T_{MR}) is found. Third, the second-stage IDT versus mixture fraction profiles are plotted again for each blend by assuming that both the HRF and LRF streams are at a similar $T = T_{MR}$. Fourth, for each blend, the point with $\tau_2 = 1$ ms on the new IDT versus mixture fraction profile is selected and its initial temperature (T_{init}) and mixture compositions are extracted, which are reported in Table 1 for each blend. Here, Y_s^{ave} denotes the mass fraction value, where s indicates the species name. We note that detailed justifications on the utilized methodology for defining the initial mixture conditions are available in Ref. [59]. However, two important points are mentioned here to better justify the assumptions in the adopted methodology. First, DF spray simulations indicate that ignition starts around the most reactive mixture fraction and within one millisecond time frame, see e.g. [83]. Second, recent studies [46,84] have provided numerical evidence on the dominant role of mixture stratification compared to thermal stratification on the reactivity stratification in DF mixtures. Therefore, homogeneous temperature and $\tau_2 \approx 1$ ms are assumed in this study.

Laminar flame speed (S_l), flame thickness (δ_f) and flame temperature (T_b) for the three selected blends in Table 1 are calculated using the planar 1D premixed flame model in Cantera at engine-relevant conditions (T_{init} , $p = 60$ bar), which are reported in Table 2. Since hydrogen is known to be of a high diffusivity character, three diffusion models are used for the calculation of S_l and δ_f : multi-component (MC), mixture-averaged (MA) and unity Lewis ($Le = 1$) models. As expected, the results are similar between the models for DF-x0 since no

Table 2

Laminar flame properties from the 1D premixed flame calculations in Cantera for the three DF blends in Table 1. MC, MA, and $Le = 1$ stand for multi-component, mixture-averaged, and unity Lewis diffusion transport models, respectively.

	p (bar)	T_{init} (K)	S_l (m/s)			δ_f (μm)			T_b (K)
			MC	MA	$Le = 1$	MC	MA	$Le = 1$	
DF-x0	60	821	0.71	0.7	0.68	10.43	10.33	10.11	2524.7
DF-x0.8	60	809.5	1.28	1.25	1.23	7.09	7.07	7.16	2693.5
DF-x1	60	804	1.72	1.7	1.6	5.78	5.78	6.20	2627.7

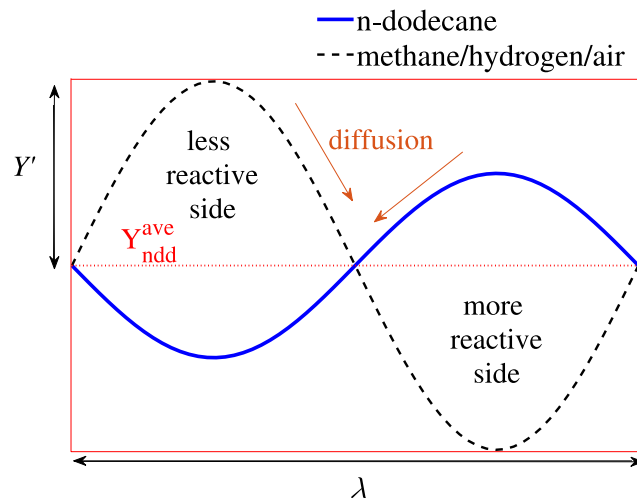


Fig. 1. Initial profiles of *n*-dodecane (HRF) and methane/hydrogen/air premixed mixture (LRF) in 1D for laminar cases. Diffusion reduces the stratification levels. The mixture ignites at the more reactive side with higher *n*-dodecane concentration. After ignition, either deflagration or autoignitive fronts are formed on the less reactive side.

hydrogen enrichment is considered. With hydrogen enrichment, i.e. in DF-x0.8 and DF-x1, the results of the unity Lewis model depart from those of the MC and MA models. However, the MA model results are close to that of the MC model. Therefore, in the following numerical simulations, the MA model is used in all 1D numerical simulations. In 3D numerical simulations, however, since only DF-x0 is considered (i.e. no hydrogen enrichment) the unity Lewis model is used to mitigate the computational costs.

2.2. Stratified mixture setup in 1D and 3D

For each considered blend in Table 1, the mixture composition is fluctuated around the average mass fraction value (Y_s^{ave}) in Table 1 using a sinusoidal distribution with λ and Y' parameters as the wavelength and amplitude of the sinusoidal profile, respectively. In this work, normalized Y' is represented by Y'_{norm} . Fig. 1 portrays the schematic profiles of the initial HRF and LRF distribution and the diffusion effect in reducing the stratification level before ignition. It is expected that ignition starts at the more reactive side where a higher amount of the HRF is present. After ignition, based on the level of stratification at the time of ignition, deflagration or autoignition fronts form on the less reactive side, where a higher amount of the LRF is present.

In 1D, mass fraction of *n*-dodecane along the physical distance (x) is initialized by

$$Y_{ndd}(x) = Y_{ndd}^{ave} + Y' \sin(kx), \quad (1)$$

where $k = 2\pi/\lambda$ is the wavenumber.

In 3D, mass fraction of *n*-dodecane is initialized by

$$Y_{ndd}(x, y, z) = Y_{ndd}^{ave} + Y' \sin(kx) \sin(ky) \sin(kz). \quad (2)$$

In both 1D and 3D, other species are initialized with a reverse sinusoidal function around their average mass fraction values. We remind that homogeneous initial temperature (T_{init}) and pressure (60 bar) are considered in both 1D and 3D numerical simulations, as justified earlier.

2.3. Numerical solver and chemical mechanism

The modified OpenFoam solver described thoroughly in Refs. [85, 86] and used previously in Ref. [59] is utilized for all numerical simulations in this study. In 1D numerical simulations, the mixture-averaged diffusion model implemented in reactingDNS is utilized. This implementation is previously used for the study of *n*-heptane/air laminar premixed flames in a low-temperature ignition regime [87], spherical laminar premixed flames with intrinsic flame instability [88], turbulent flames propagation and ignition [89,90], and ammonia/methane/air premixed laminar burner flames [91]. For 3D numerical simulations, the unity Lewis model, similar to that in our previous work [59] is used. Due to the similarity of the solver setup and assumptions to that in Ref. [59], further details are not provided herein.

The reduced chemical kinetics mechanism by Frassoldati et al. [92] is employed in this work. This chemical kinetics mechanism contains 96 species and 993 reaction steps and it is used for both 1D and 3D numerical simulations in the present work. A detailed validation of this chemical mechanism for methane/hydrogen blends with *n*-dodecane is provided in Ref. [75].

2.4. Theoretical combustion mode diagram (β -curve)

In this section, a summary of the developed theoretical analysis by Karimkashi et al. [59] is provided. This analysis is used along with the numerical simulations in the following parts. According to Sankaran et al. [29], the non-dimensional number β prescribes the border between the deflagration and spontaneous (autoignition) modes and it is originally defined as the ratio of the laminar flame speed (S_l) to the ignition wave speed (S_{ign}). S_{ign} is defined as the inverse of the second-stage IDT (τ_2) gradient according to Zeldovich [4]. When $\beta < 1$ or $S_{ign} > S_l$, the propagation speed is higher than the laminar flame speed and the combustion mode is spontaneous. On the contrary, when $\beta > 1$ or $S_{ign} \leq S_l$, the combustion mode is deflagration. We note that in this work, τ_2 which corresponds to the initiation of high-temperature chemistry (HTC) is considered as the main ignition event. However, the first-stage IDT (τ_1), which indicates the initiation of low-temperature chemistry (LTC), is also reported in the results part.

In Ref. [59], a theoretical analysis for DF mixtures with initially homogeneous temperature and pressure was developed in a time-dependent diffusion–reaction problem. An analytical expression was provided for β in the (Y' , λ) parameter space, where Y' and λ were the initial stratification amplitude and wavelength, respectively, in a sinusoidal mixture profile with periodic boundary conditions. The provided expression for laminar conditions is

$$Y' = \frac{\beta \lambda \exp(4\pi^2 \nu \tau_2 / \lambda^2)}{C_\beta S_l \alpha 2\pi} \quad (3)$$

In Eq. (3), ν and C_β represent the kinematic viscosity and a constant of unity order, respectively. We note that for simplicity, ν is assumed to be equivalent to the mass diffusivity (unity Schmidt number assumption) and $C_\beta = 1$ is considered in this work. Moreover, α is the slope of linearized variations of τ_2 against mixture fraction (Z), which is found from the 0D mixing line concept calculations, as explained earlier in Section 2.1.

The expression in Eq. (3) was improved to consider effects of convection due to turbulence by replacing ν with $\nu_{eff} = \nu + \nu_t$, wherein ν_t is the turbulence diffusivity (under unity Schmidt number $\nu_t = D_t$). It was justified that $\nu_t = l_t \times u_t$, in which l_t and u_t represent the

initial turbulence length-scale and velocity, respectively [61]. The final expression under turbulent conditions is

$$Y' = \frac{\beta \lambda \exp(4\pi^2 (\nu + \nu_t) \tau_2 / \lambda^2)}{C_\beta S_l \alpha 2\pi} \quad (4)$$

The expression in Eq. (4) was validated at different turbulence levels using 2D fully-resolved numerical simulations in Ref. [59]. Here, the reported values using the MA model in Table 2 are used as inputs in Eqs. (3) and (4).

3. Part 1: Laminar 1D cases and results

3.1. Laminar 1D cases

To define the laminar 1D simulation points, $\beta = 1$ profiles (c.f. Eq. (3)) are plotted in Fig. 2 in the (λ , Y') space for each of the three considered blends in Table 1. We remind that the region above (below) each profile indicates the deflagration (spontaneous) region for the considered blend under laminar conditions. The plotted β -curves reveal the region of interest in the (λ , Y') space for the simulation points. Therefore, 1D laminar simulation points are defined around $\beta = 1$ with variations of $\lambda/\lambda_{diff} = [0.2, 0.316, 0.5, 1]$ and $Y'_{norm} = [0.02, 0.05, 0.2, 0.5, 1]$. Consequently, 20 points in the (λ , Y') space (displayed with circles in Fig. 2) are defined for each of the three considered blends in Table 1 to carry out transient 1D numerical simulations; i.e. 60 1D simulations in total. The diffusion length-scale ($\lambda_{diff} = 2\pi\sqrt{\nu\tau_2}$) for the three considered blends is 0.63 mm ($\nu = 10^{-5}$ m²/s and $\tau_2 = 1$ ms). The considered grid resolution in all of the 1D simulations is 0.25 μ m, which satisfies at least 20 grid points within the respective flame thickness of each mixture; c.f. the flame thickness values reported for each mixture in Table 2.

Considering the demonstrated $\beta = 1$ profiles in Fig. 2, it is observed that adding more hydrogen to the premixed charge of the LRF/air expands the flame propagation region compared to the spontaneous region. This observation suggests that adding hydrogen can lead to higher propensity of flame propagation at similar stratification levels, which is consistent with lower reactivity of H₂/air compared to CH₄/air at temperatures below 1000 K at 60 bar and equivalence ratio 0.5, according to the 0D analysis in Ref. [75]. Next, we evaluate the combustion mode predictions of the β -curve theory using 1D numerical simulations.

3.2. Results and discussions: 1D laminar

3.2.1. 1D simulations: combustion mode

To distinguish between the deflagration or spontaneous combustion modes in 1D numerical simulations, the same evaluation methodology used in Ref. [59] is considered. This qualitative evaluation is based on the expectation for a high temperature gradient in a deflagrative front (in the order of its respective 1D laminar flame) compared to an autoignitive front, and it is useful when a large number of simulations need to be evaluated. First, at each time instance after ignition, the difference between the maximum and minimum temperature in the domain (ΔT) is calculated and its maximum value in time (ΔT_{max}) is found. Second, ΔT_{max} is compared with a threshold temperature difference ΔT_{th} . Here, considering $T_b - T_{init}$ in Table 2, $\Delta T_{th} = 1700$ K is considered. Third, if $\Delta T_{max} \geq \Delta T_{th}$ and if $\Delta T \geq \Delta T_{th}$ remains valid for three consecutive time-steps of 1 μ s after reaching ΔT_{max} , the combustion mode is evaluated as deflagration. Otherwise, it is considered as spontaneous. The evaluation over several consecutive time-steps is essential to make certain that the formed flame-like front is not a momentary phenomenon right after ignition. However, we note that considering three time-steps is an arbitrary choice here.

Following the above-mentioned evaluation, combustion modes of the simulation points are identified, which are indicated with different

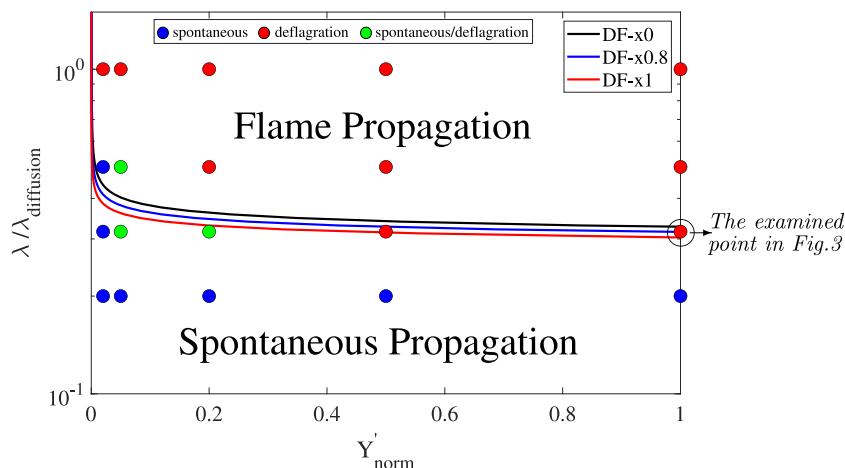


Fig. 2. Combustion mode diagram for DF blends under laminar conditions ($C_\beta = 1$, $\beta = 1$). Circles mark initial λ and Y' for 1D numerical simulations ($P = 60$ bar). For each point, three simulations are carried out: DF-x0, DF-x0.8, and DF-x1. Blue and red colors denote the spontaneous and deflagration modes for the three DF simulations, respectively. Green color presents the spontaneous mode for DF-x0 and the deflagration mode for DF-x0.8 and DF-x1. (For interpretation of the references to color in this figure legend, the reader is referred to the web version of this article.)

colors of the circles in Fig. 2. Blue and red colors denote spontaneous and deflagration combustion modes, respectively. The points with green color, present the deflagration mode for DF-x0.8 and DF-x1 blends, while the spontaneous mode for DF-x0. Overall, there is a fair consistency for the combustion mode predicted by the theory ($\beta = 1$ in Eq. (3)) and resulted from the 1D numerical simulations. Moreover, hydrogen enrichment of the LRF switches the combustion mode of the three test cases close to the $\beta = 1$ borderlines (displayed with green color) from spontaneous to deflagration.

3.2.2. 1D simulations: transport budget analysis

Next, we select one point in the vicinity of the borderlines ($\beta = 1$) to elucidate the differences between the three considered blends. The selected point with $\lambda/\lambda_{diff} = 0.316$ and $Y'_{norm} = 1$ is marked in Fig. 2. As a remark, points far away from the borderlines are less attractive since they demonstrate similar combustion modes for the three blends. Fig. 3 displays the progress of temperature as well as the diffusion and reaction terms of the energy equation (budget analysis) with time along the domain axis normalized by $k_{diff} = 2\pi/\lambda_{diff}$ at the selected point in Fig. 2 for DF-x0 (upper row), DF-x0.8 (middle row), and DF-x1 (lower row). Note that the diffusion and reaction terms are normalized with the maximum value of the reaction term in time. It is observed from the temperature profiles that in all cases, ignition happens at the more reactive side of the domain (number 0) and after a transitional period (numbers 1 and 2), flame-like fronts are formed in the less reactive side of the domain (c.f. Fig. 1). Moreover, the budget analysis shows that after flame-like fronts are formed (number 3 onward) the diffusion and reaction terms are in the same order of magnitude, which confirms that deflagrative fronts are formed. We note that the maximum peak of the reaction term and the minimum peak of the diffusion term are closer to each other in DF-x1 compared to DF-x0.8 to DF-x0, which may imply that adding more hydrogen to the LRF mixture leads to the promotion of the deflagration mode. This is consistent with the theoretical β -curve prediction in Fig. 2, wherein the flame propagation zone was noticed to expand slightly by hydrogen enrichment.

According to the numerical results, τ_2 is 0.88, 0.67, and 0.69 ms at the selected simulation point for DF-x0, DF-x0.8, and DF-x1, respectively. Therefore, by adding hydrogen, IDT is advanced from DF-x0 to DF-x0.8 and delayed from DF-x0.8 to DF-x1. However, IDT variations are insignificant. In addition, we define the combustion duration as $\delta\tau = \tau_{end} - \tau_2$, where τ_{end} is the ending time of the combustion process defined as when the maximum temperature crosses 3000 K across the domain. At the selected point, $\delta\tau = 0.135$, 0.019, and 0.0148 ms for DF-x0, DF-x0.8, and DF-x1, respectively. Therefore, replacing methane by

hydrogen shortens the combustion duration ≈ 9 times, which is mainly due to the faster propagation speed of the hydrogen flame compared to the methane flame, c.f. Table 2. It should be noted that in Fig. 3, the time intervals between the plotted reaction fronts are 4, 3, and 2 (μ s) for DF-x0, DF-x0.8, and DF-x1, respectively.

As a final remark in this part, we note that the mixture-averaged (MA) diffusion model was used in all of the 1D numerical simulations in this section. However, all the simulations were conducted with the unity Lewis model as well. The results of Fig. 3 using the unity Lewis model are presented in Appendix A. It was found that for DF-x0, the simulation results using both the MA and unity Lewis models are very similar. For DF-x0.8 and DF-x1, although the quantitative results such as IDT and $\delta\tau$ differ, the identified modes of combustion are not affected. Overall, effects of hydrogen diffusion in changing the combustion mode in the studied cases is limited due to the fact that ignition happens within a short period after the simulations start and also that the mass fraction of hydrogen in the entire mixture is small compared to the other fuels present in the mixture (c.f. Table 1).

In the following part of the paper, effects of turbulence intensity on the combustion mode is studied in 3D. However, only DF-x0 (no hydrogen enrichment) is considered due to the high computational requirements of the 3D cases with hydrogen. More details are provided in the following section. We note that considering the 1D results, effect of hydrogen enrichment on switching the combustion mode is expected to be of minor importance under turbulent conditions.

4. Part 2: Turbulent 3D cases and results

4.1. Turbulent 3D cases

In this section, effects of turbulence intensity on the combustion mode is explored. In 3D turbulent cases, only DF-x0 mixture (no hydrogen in the LRF blend) is studied in this work due to two main reasons. First, the laminar flame thickness of pure hydrogen/air at the considered initial conditions ($p = 60$ bar, $T = T_{mit}$, $\phi = 0.5$) is ≈ 10 μ m, which is ≈ 5 times thinner than that of pure methane/air (≈ 50 μ m) at similar conditions. Therefore, resolving the flame in 3D simulations that contain hydrogen (DF-x0.8 or DF-x1) is infeasible with our current numerical resources, considering the large chemical mechanism used in this work. Second, when there is hydrogen enrichment in the mixture, effects of hydrogen preferential diffusion should be considered by using a non-unity Lewis transport model, which adds to the computational resources requirements. Therefore, we do not investigate DF-x0.8 and

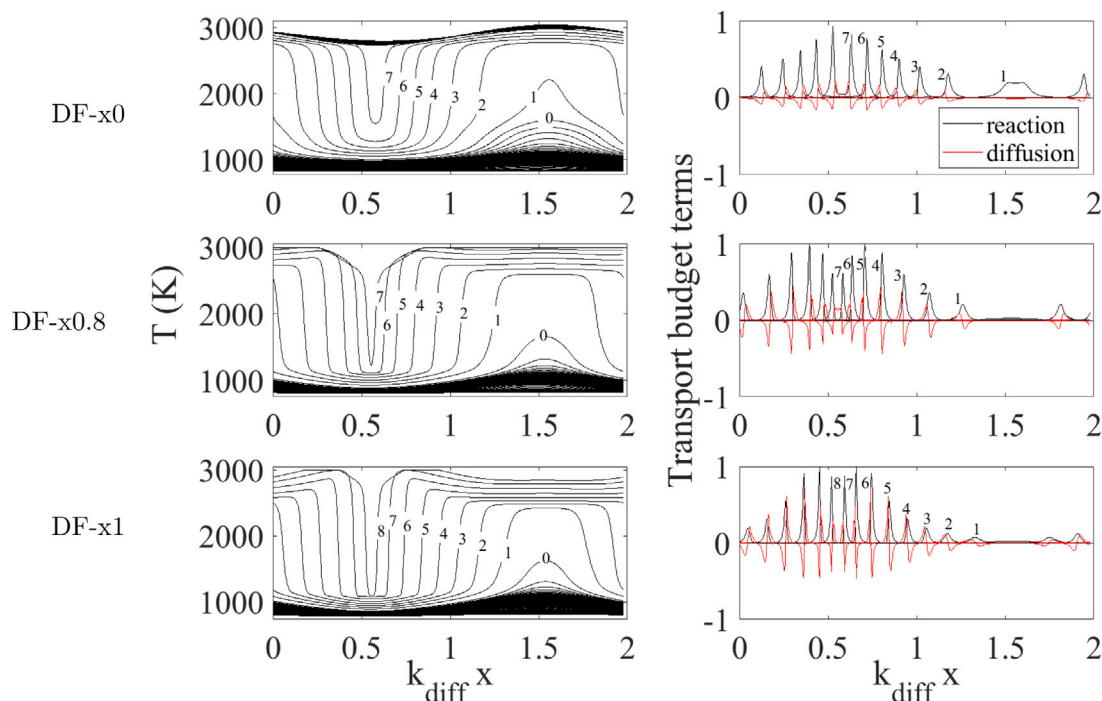


Fig. 3. Time evolution of the reaction fronts for the selected point in Fig. 2 ($\lambda/\lambda_{diff} = 0.316$ and $Y'_{norm} = 1$) for DF-x0 (upper row), DF-x0.8 (middle row), and DF-x1 (lower row) under laminar conditions. Numbers represent time intervals of 4, 3, and 2 (μs) for DF-x0, DF-x0.8, and DF-x1, respectively. Number 0 represents a cluster of time-steps corresponding to the ignition kernel formation phase. (For interpretation of the references to color in this figure legend, the reader is referred to the web version of this article.)

DF-x1 mixtures under turbulent conditions in this work. Here, only DF-x0 using the unity Lewis approach is considered since the 1D laminar cases rendered no significant differences between the results of the unity Lewis and MA models for DF-x0 (c.f. Appendix A).

It should be noted that in the following 3D simulations, we assume that the required grid resolution for resolving the flame is ≈ 10 – 15 grid points within the laminar flame thickness of the 1D premixed LRF/air flame under relevant initial conditions. For instance for DF-x0, the laminar flame thickness of the premixed pure methane/air flame at $T = 821$ K, $p = 60$ bar, and $\phi = 0.5$ is considered, which is ≈ 50 μm . This value is ≈ 5 times thicker than the one reported in Table 2 for the premixed *n*-dodecane/methane/air flame. This assumption is considered following the 1D simulation results which suggest that the formed deflagrative fronts mainly contain the LRF since the majority of the HRF (here *n*-dodecane) is consumed in the system at the initial ignition phase. More details can be found in Ref. [59]. In addition, our following results of the 3D turbulent cases demonstrate that this grid resolution is sufficient for resolving the DF-x0 flames since the temperature gradients are captured properly across the flame fronts.

To define the initial conditions for 3D turbulent simulations, first, we plot the combustion mode diagram, i.e. $\beta = 1$ in Eq. (4), under similar conditions for DF-x0 but with various turbulence diffusivity (ν_t). The profiles are displayed in Fig. 4. The region above (below) each $\beta = 1$ profile indicates the deflagration (spontaneous) region for each turbulence diffusivity. As expected, increasing turbulence velocity, and accordingly ν_t , leads to the expansion of the spontaneous region due to higher levels of mixing by stronger turbulence. Second, we select one simulation point in the (λ, Y') space for 3D turbulent numerical simulations. The point (marked in Fig. 4) is selected such that it lies within both the autoignition and deflagration zones for different ν_t . The stratification characteristics of the point are $\lambda/\lambda_{diff} = 1.59$ or $\lambda = 1$ mm and $Y'_{norm} = 1$. Note that although larger λ values might be interesting for numerical simulations, this is the largest λ that we can afford with the current computational resources since the computational domain is a cube of size $L = \lambda$ in each direction and a larger λ means a larger domain size.

Table 3

Characteristics of 3D turbulent case studies of DF *n*-dodecane/methane. Turbulence diffusivity ($\nu_t = l_t \times u_t$) and initial Kolmogorov length-scale are reported.

Turbulent cases	l_t (mm)	u_t (m/s)	ν_t (m^2/s)	η (μm)	Re_t
Case I	0.1	1	1×10^{-4}	17.8	10
Case II	0.1	10	1×10^{-3}	3.2	100
Case III	0.1	50	5×10^{-3}	0.95	500
Case IV	0.1	100	1×10^{-2}	0.56	1000

Next, we provide details on the setup for 3D turbulent cases. In 3D turbulent simulations, uniform initial temperature ($T_{init} = 821$ K) and pressure (60 bar) are considered in all cases similar to the 1D cases. The initial turbulence length-scale (l_t) is kept constant at $0.1 \times L$ while the initial turbulence velocity (u_t) is increased as reported for the listed cases I–IV in Table 3. The resulting ν_t values are those plotted in Fig. 4. Turbulent Reynolds number is defined as $Re_t = u_t \times l_t / \nu$, which varies between 10^4 – 10^6 in cases I–IV.

Fig. 5(a) displays the initial 3D field of *n*-dodecane mass fraction at the selected point using Eq. (2). The domain is a cube of size $L = 1$ mm and periodic boundary conditions are considered for all boundaries. Isotropic homogeneous and decaying turbulence is initialized with an initial turbulent kinetic energy spectrum function by Passot–Pouquet [79], described for instance in Ref. [93], using the Python tool provided in Refs. [94–96]. Fig. 5(b) shows the initial velocity field in case II as a demonstration example.

The grid resolution is 4 μm in all of the considered test cases, i.e. 250 grid points in each direction. This resolution can resolve the flame thickness of the methane flame at the considered initial conditions in cases I–IV (≈ 50 μm ; c.f. the earlier notes in this section). On the other hand, the estimated initial Kolmogorov length-scale ($\eta = (\nu^3/\epsilon)^{0.25}$, where $\epsilon = u_t^3/l_t$) of each case study is reported in Table 3. The considered resolution is only smaller than the estimated η in case I. However, considering the large chemical mechanism used in this work, a finer grid resolution in cases II–IV is infeasible due to the high computational

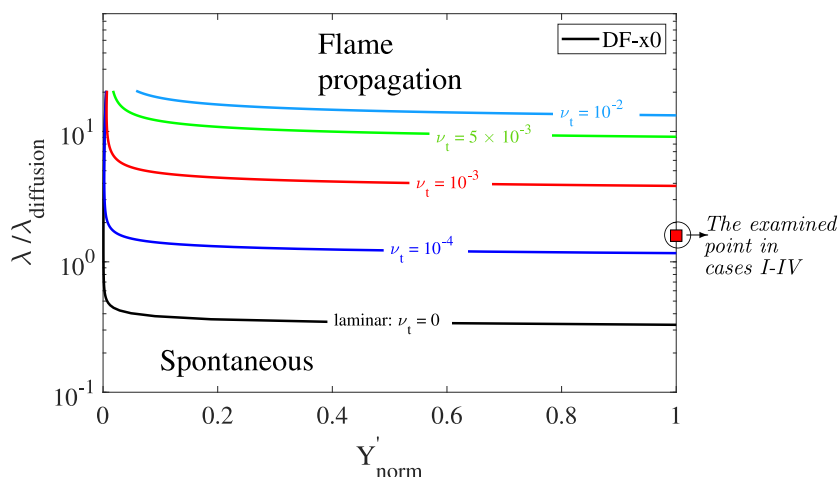


Fig. 4. Combustion mode diagrams ($\beta = 1$ in Eq. (4)) for turbulent conditions considered in cases I–IV. Stronger turbulence leads to higher turbulence diffusivity (ν_t) and hence, stronger mixing and prevalence of the spontaneous region. The unit of ν_t in the figure is m^2/s . The marked point is considered for 3D simulations in cases I–IV for DF-x0 (no hydrogen enrichment).

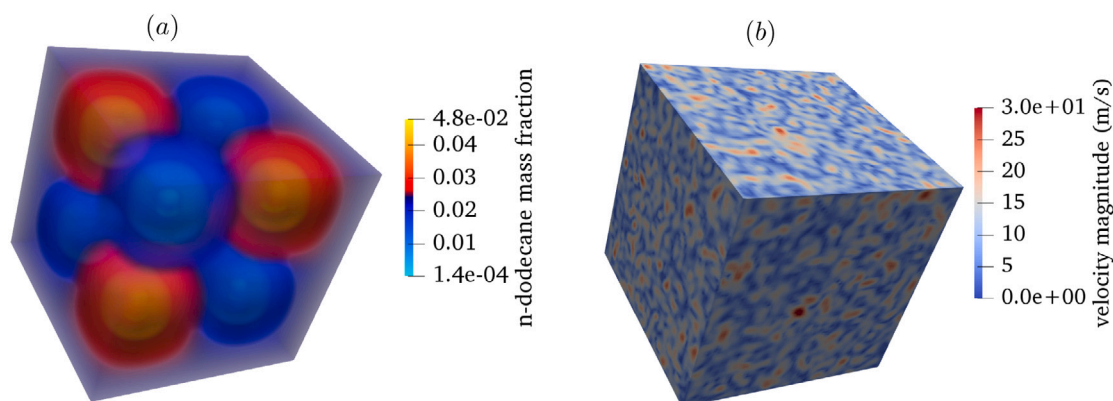


Fig. 5. Initialization fields of *n*-dodecane mass fraction (a), and velocity magnitude for one of the considered cases (case II) (b) in 3D numerical simulations. The velocity field is initialized with an initial turbulent kinetic energy spectrum function by Passot–Pouquet [79].

costs of these case studies. Therefore, cases II and III which are the main focus of our analyses in the following sections are only flame-resolved. We note that there are similar recent works in the literature which rely on the flame-resolved simulations considering the current limitations of the computational resources, see e.g. [97,98]. On the other hand, since decaying turbulence is used in the present work, kinetic energy dissipates quickly after the simulations start and the turbulence length-scales increase significantly. This effect might reduce the disparity of our current results with potentially fully-resolved simulations in future, especially since chemical reactions do not kick in initially (before the first-stage ignition) in these cases. For the sake of completeness, a short analysis on the energy dissipation rate in the considered cases is provided in Appendix B.

Finally, it is noteworthy that considering the combustion mode diagrams by the theory, it is expected to observe deflagration fronts in case I and autoignition fronts in cases II–IV. However, the simulation results present a different trend for case II, which is further explored and discussed in the following.

4.2. Results and discussions: 3D turbulent

4.2.1. 3D turbulent simulations: Global metrics

In this section, first, we identify the combustion mode in cases I–IV based on the global metrics including HRR and $\delta\tau$. Table 4 outlines the

statistics obtained from 3D numerical simulations of cases I–IV. Here, τ_2 and $\delta\tau$ have similar definitions to those provided earlier. Also, Z_{min} , Z_{max} , and Z_{ave} represent the minimum, maximum and average mixture fraction across the domain at τ_2 . According to the results of Table 4, although ignition time (τ_2) in case I is around half of that in cases II–IV, cases I and II have an order of magnitude longer combustion duration ($\delta\tau$) compared to cases III and IV. As a note, it is expected that autoignition fronts have at least an order of magnitude faster propagation speed than deflagration fronts, and therefore, a shorter combustion duration in the spontaneous mode compared to the deflagration mode. The reported $\delta\tau$ values imply that the combustion mode is spontaneous in cases III and IV, while the deflagration mode prevails in cases I and II. Consistently, the range of mixture fraction fluctuations around Z_{ave} at τ_2 in cases I and II is considerably broader than that in cases III and IV, which demonstrates that stronger turbulence in cases III and IV has led to faster mixing, i.e. promotion of the spontaneous combustion mode. We note that Z_{ave} is identical for all cases at 1.6×10^{-2} , due to the similarity of the initial mixture stratification in cases I–IV.

Fig. 6 displays temporal evolution of the maximum heat release rate (HRR_{max}), arithmetic mean (field-averaged) pressure (p_{ave}), and maximum temperature (T_{max}) across the domain for cases I–IV. Note the logarithmic scale of HRR_{max} in the figure. The first-stage IDT (τ_1), which is identified as the first peak of T_{max} and corresponds to the initiation of LTC, is marked with blue circles. More details on the definition of τ_1 in DF mixtures are provided in Refs. [41,42,75]. As a

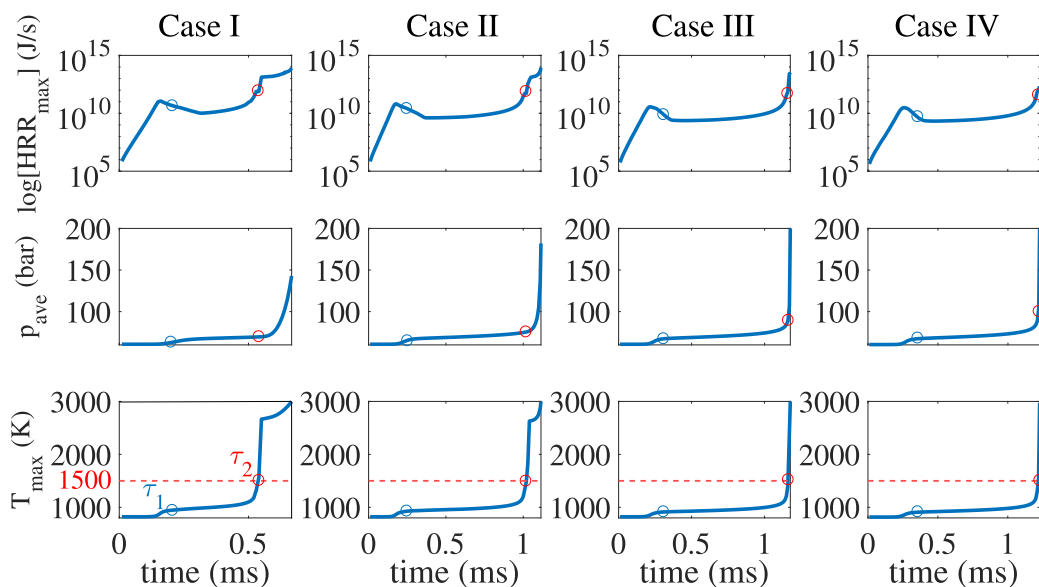


Fig. 6. Temporal evolution of the maximum heat release rate (HRR_{max}), field-averaged pressure (p_{ave}), and maximum temperature (T_{max}) across the domain for cases I–IV. Note the logarithmic scale of the heat release rate profiles. The HRR is noted to abruptly increase in cases III and IV compared to cases I and II. Blue and red circles depict τ_1 and τ_2 , respectively. Red dashed lines mark $T_{max} = 1500$ K. (For interpretation of the references to color in this figure legend, the reader is referred to the web version of this article.)

Table 4

Statistics of the turbulent numerical simulations results, where IDT (τ_2), combustion duration ($\delta\tau$) and variation of the mixture fraction (Z) at τ_2 are reported.

Case	Mode	τ_2 (ms)	$\delta\tau$ (ms)	Z_{min}	Z_{max}	Z_{ave}
Case I	Deflag.	0.54	0.127	2.6×10^{-5}	3.2×10^{-2}	1.6×10^{-2}
Case II	Deflag.	1.02	0.095	1.3×10^{-2}	1.9×10^{-2}	1.6×10^{-2}
Case III	Spont.	1.17	0.0071	1.56×10^{-2}	1.63×10^{-2}	1.6×10^{-2}
Case IV	Spont.	1.22	0.0078	1.57×10^{-2}	1.61×10^{-2}	1.6×10^{-2}

remark, in this work, only the second-stage IDT (τ_2) is of our interest as the main ignition event in the theory and other analyses. Here, τ_2 (relevant to the initiation of HTC) is defined as when $T_{max} = 1500$ K and it is marked with red circles in Fig. 6.

According to Fig. 6, in cases I–IV, HRR_{max} grows rapidly until τ_1 , due to the activation of LTC reactions leading to the slight increase of both T_{max} and p_{ave} at τ_1 . These LTC reactions decompose *n*-dodecane and produce adequate OH radicals for the onset of the second-stage ignition. After τ_1 , there is a slight decrease in HRR_{max} which corresponds to the dominance of inhibiting reactions that reduce the overall reactivity as discussed in Ref. [75]. Within the time period between τ_1 and τ_2 , temperature and pressure increase gradually. At τ_2 , there is an abrupt rise in HRR_{max} , due to the initiation of HTC reactions leading to the major increase of both T_{max} and p_{ave} . Considering the identical threshold for τ_{end} in cases I–IV (i.e. reaching maximum 3000 K across the domain), it is observed in Fig. 9 that in cases III and IV, the time window between τ_2 and τ_{end} is considerably shorter than the one in cases I and II, as also reported in Table 4.

While the provided global metrics in this section imply the deflagration and spontaneous combustion modes in cases I–II and III–IV, respectively, a detailed analysis of the 3D data is essential to identify the combustion modes and their characteristics. In the remainder of this work, case II (deflagration) and case III (spontaneous) are further analyzed to provide details on the mixing and flame initiation phenomena in DF mixtures. Fig. 7 shows the volume-rendered data of heat release rate (HRR) at slightly after the ignition time ($\approx \tau_2$) in cases II (left) and III (right). It is observed that in case II, several ignition pockets of high HRR values are formed in different sizes at various locations in the domain. However, a large proportion of the mixture is still at low HRR values and non-ignitive. In this case, which is in the deflagration mode, ignition pockets grow and form several

self-propagating deflagration fronts. Eventually, the deflagration fronts merge until the entire mixture is burnt. On the other hand, in case III, although a single ignition pocket is present, the whole mixture is at relatively high HRR values and ready to autoignite, leading to spontaneous combustion. In the following section, further details are provided on the differences between cases II and III.

4.2.2. 3D Turbulent simulations: transport budget analysis

Based on the discussion in the previous part, deflagration and spontaneous combustion modes are expected for cases II and III, respectively. In order to confirm this, a budget analysis of the energy equation terms is provided for cases II and III in what follows. In Fig. 8, time evolution of the temperature field cutplanes in case II is presented. The starting time ($t = 1.04$ ms) is slightly after the second-stage ignition in case II ($\tau_2 = 1.02$ ms). The following cutplanes are presented in 0.02 ms intervals until τ_{end} . It is observed that first, pockets of high temperature (ignition kernels) are formed and then, the pockets gradually expand and merge ($t = 1.06$ and 1.08 ms) to complete the combustion process ($t = 1.11$ ms). The diffusion (D) and the reaction (R) terms of the energy equation are plotted along certain investigation lines A–D normal to the flame front in the 3D space while the 2D planes containing the investigation lines are shown. It is noted that diffusion and reaction are in the same order of magnitude at different time instances after τ_2 along various investigation lines. This analysis confirms the previous observation in earlier parts that the combustion mode in case II is deflagration. Note that the diffusion and the reaction terms are normalized by the maximum value of the reaction term at each time instance while the *x*-axis shows the normalized arc length of each investigation line. The temperature profiles along the investigation lines are also plotted, which depict laminar flame-like structures as expected for the deflagration fronts. It is noted that since decaying turbulence is considered in this work, turbulence intensity in all of the considered cases is relatively low at the ignition time and laminar flame-like structures are expected in the deflagration combustion mode. We note that the temperature profiles indicate that the considered grid resolution in this case study is sufficient to resolve the flame since the temperature gradients are properly captured.

Similarly, Fig. 9 presents time evolution of the temperature field cutplanes in case III as well as the transport budget analysis along selected investigation lines A–C. Although the starting time ($t = 1.16$ ms)

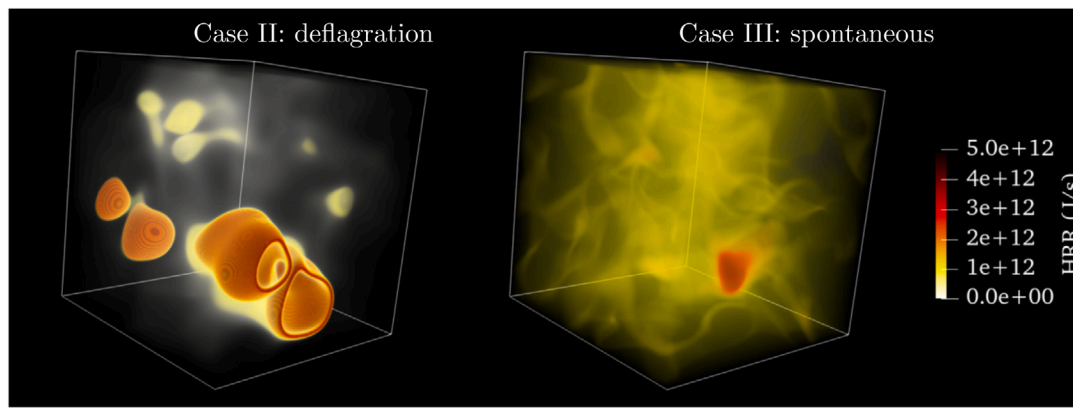


Fig. 7. Volume-rendered 3D data of the HRR at the time of ignition in cases II (left) and III (right). In case II (deflagration), ignition pockets of high HRR values with different sizes are formed while the rest of mixture remains at low (almost zero) HRR values. In case III (spontaneous), while a single pocket with high HRR is observed, the rest of mixture is also at relatively high HRR values and prone to ignite spontaneously.

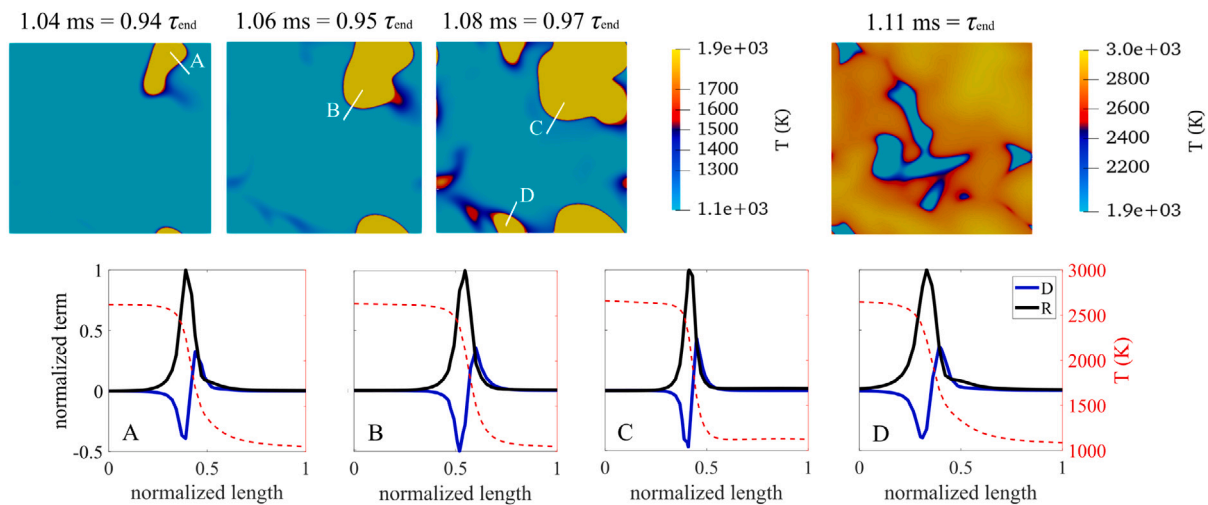


Fig. 8. Time evolution of the temperature field cutplanes in case II with marked investigation lines A-D, normal to the flame front (top row). The transport budget analysis and temperature profiles along the investigation lines A-D are shown in the bottom row. Blue and black lines represent diffusion (D) and reaction (R), respectively. The combustion mode is deflagration. (For interpretation of the references to color in this figure legend, the reader is referred to the web version of this article.)

is slightly before the second-stage ignition in case III ($\tau_2 = 1.17$ ms), the entire mixture is already at high temperature ($1200 < T < 1500$). The following cutplanes are after 0.01 ms and at τ_{end} , respectively. Opposite to case II, the ignition kernel ($T > 1500$ K) forms in a very narrow time window ($t = 1.17$ ms) and only ≈ 0.007 ms after the formation of the ignition kernel, the combustion process completes ($t = 1.177$ ms). This observation is consistent with the reported short $\delta\tau$ in Table 4 for case III. The budget analysis profiles along the selected investigation lines A–C illustrate that the reaction term is dominant over the diffusion term by an order of magnitude. Moreover, the temperature profiles do not depict the laminar flame-like structures which is in contrast to the observations in case II. In particular, the temperature difference along the investigation lines is smaller than that in case II. These observations suggest that the combustion mode in case III is spontaneous as noted earlier.

4.3. Further analysis of the 3D data

In this part, we provide further analysis on the combustion mode (in particular, flame initiation) in 3D stratified DF mixtures. Finally, in the following part, a correction factor is provided for the theoretical Eq. (4) to improve its prediction of the combustion mode in 3D stratified DF mixtures. We note that it is shown in the literature that in low Karlovitz stratified flames, standard characteristics of the premixed flames are

typically valid, including alignment of the key intermediate species profiles with those of the unstrained laminar premixed flames in the progress variable space, c.f. [22,99].

4.3.1. Mixing analysis

Since in this study, methane flame initiation after ignition is studied, a progress variable (C) is defined based on methane mass fraction:

$$C = \frac{Y_{\text{CH}_4} - Y_{\text{CH}_4}^u}{Y_{\text{CH}_4}^b - Y_{\text{CH}_4}^u}, \quad (5)$$

where Y_{CH_4} , $Y_{\text{CH}_4}^u$, and $Y_{\text{CH}_4}^b$ denote methane mass fraction, unburnt methane mass fraction, and burnt methane mass fraction, respectively. We define the following flame zones based on the progress variable: $0 \leq C < 0.1$ unburnt zone, $0.1 \leq C < 0.7$ preheat zone, $0.7 \leq C \leq 0.95$ inner reaction zone, and $0.95 < C \leq 1$ burnt zone.

In Fig. 10, the probability density function (PDF) of the absolute values of the progress variable gradient ($|\nabla C|$) and mixture fraction gradient ($|\nabla Z|$), conditioned on the four defined flame zones, are presented at $0.95 \tau_{end}$ and $0.995 \tau_{end}$ for cases II and III, respectively. The selected time in each case corresponds to post-ignition (i.e. slightly after τ_2) when ignition fronts are formed as displayed in Figs. 8 and 9. There are three important points which illustrate deflagration (autoignition) in case II (III). First, all of the four flame zones are present in case II,

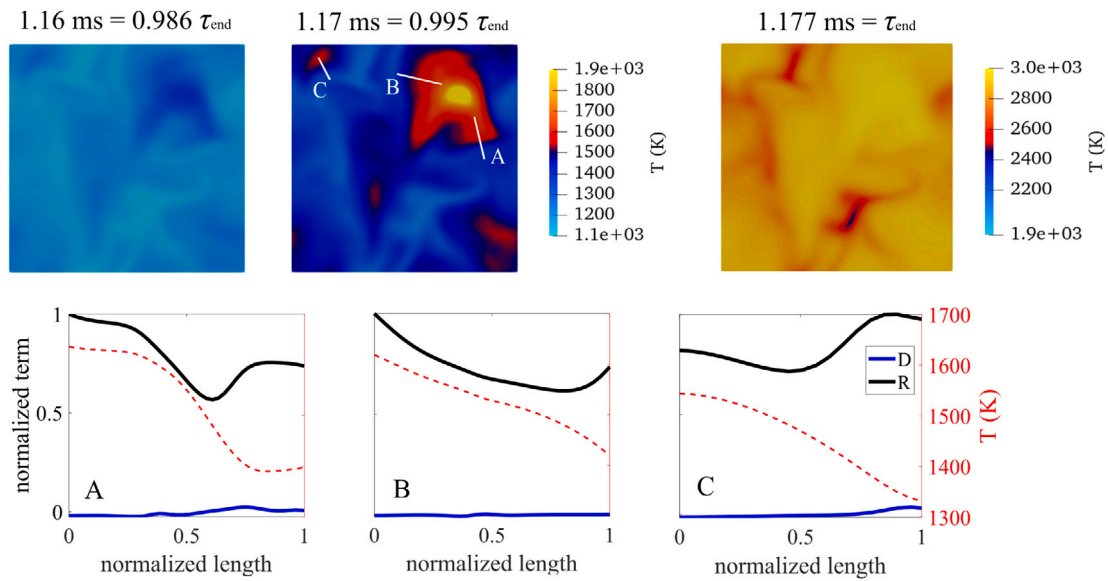


Fig. 9. Time evolution of the temperature field cutplanes in case III with marked investigation lines A-C, normal to the flame front (top row). The transport budget analysis and temperature profiles along the investigation lines A-C are shown in the bottom row. Blue and black lines represent diffusion (D) and reaction (R), respectively. The combustion mode is spontaneous. (For interpretation of the references to color in this figure legend, the reader is referred to the web version of this article.)

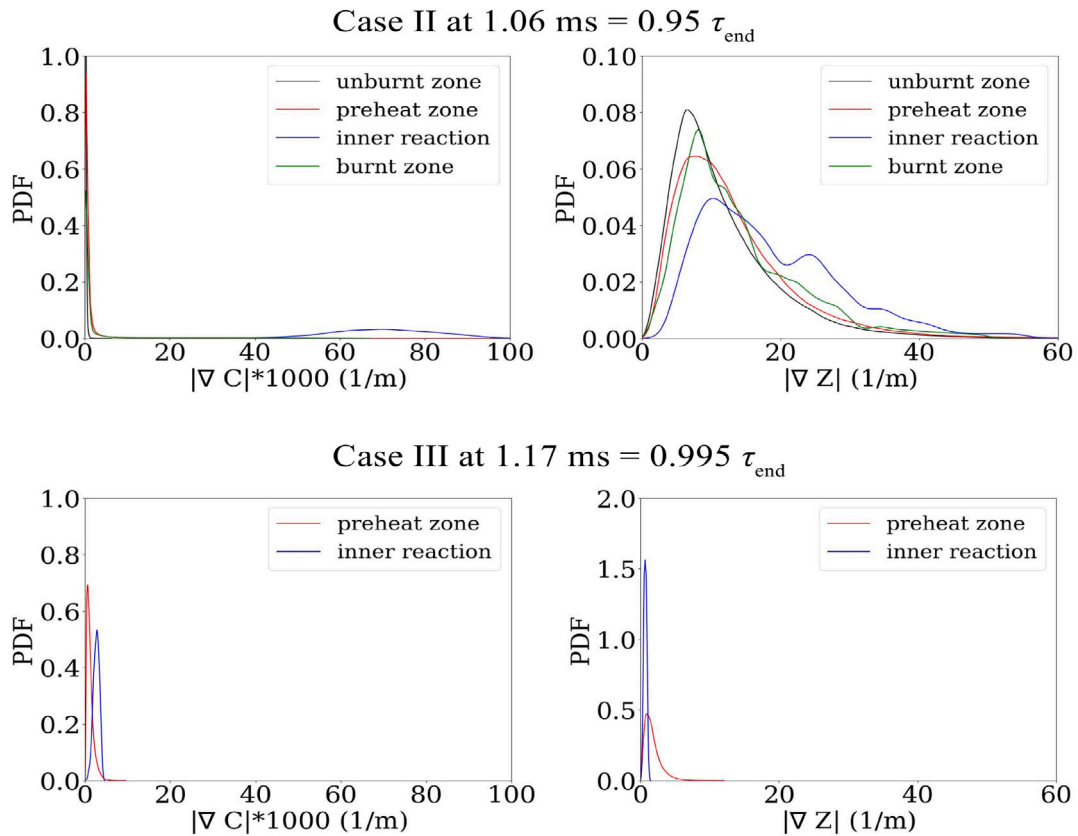


Fig. 10. PDF of the magnitudes of the progress variable gradient ($|\nabla C|$) and mixture fraction gradient ($|\nabla Z|$) in different flame zones at $0.95\tau_{end}$ and $0.995\tau_{end}$ for cases II (top) and III (bottom), respectively. Note the 1000 factor for $|\nabla C|$ in the figure. In case III, only preheat and inner reaction zones are present.

while for case III, only the preheat and the inner reaction zones exist at the shown time instance. Second, in case II, $|\nabla C|$ in the unburnt, preheat, and burnt zones is mainly distributed around small values while high $|\nabla C|$ values are observed within the inner reaction zone,

as expected in deflagrative fronts. In contrast, in case III, $|\nabla C|$ in both the preheat and the inner reaction zones is mainly distributed around small values. Third, mixture fraction gradients in case II are an order of magnitude larger and more stratified than those in case III, implying the

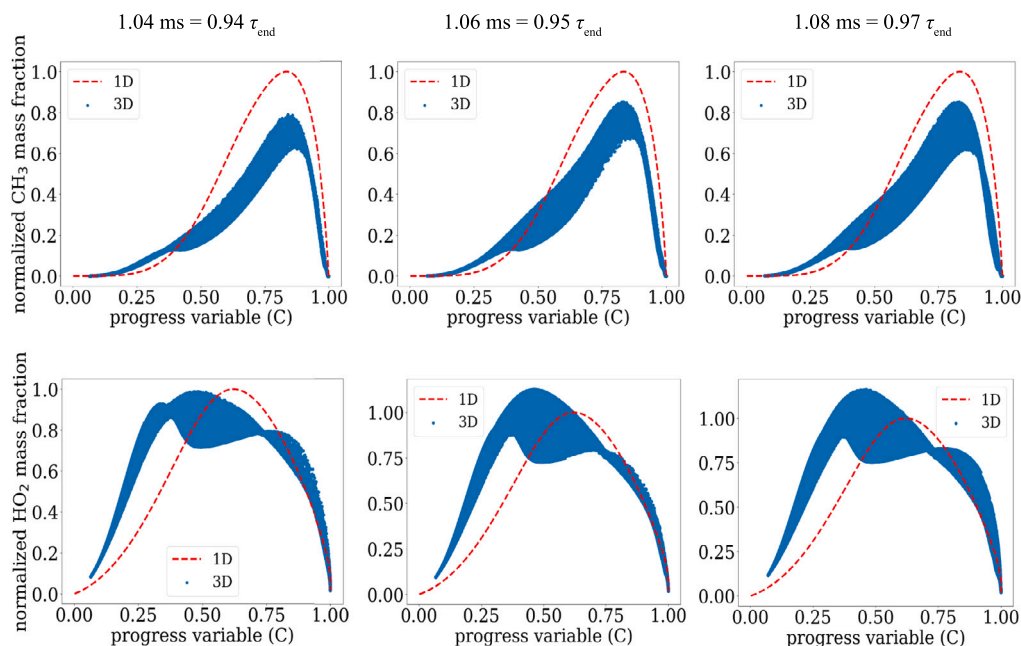


Fig. 11. Scatter data of CH_3 and HO_2 mass fractions in case II superimposed on the profiles of unstrained 1D premixed flames in the progress variable space at different time. A fair consistency between the 3D data and 1D unstrained flamelets is observed.

stratified flame onset in case II compared to the relatively homogeneous autoignition fronts in case III with an order of magnitude smaller gradients.

4.3.2. Time evolution of intermediate species

Scatter plots for mass fractions of two intermediate species CH_3 and HO_2 , relevant to premixed methane/air flames, are presented for case II in Fig. 11 and case III in Fig. 12. The scatter plots are shown in the progress variable space at different time instances discussed earlier in Figs. 8–10. In addition, mass fraction profiles of the intermediate species from the 1D numerical simulation of an unstrained premixed methane/air flame with the initial conditions of DF-x0 in Table 1 are calculated in Cantera and superimposed in both figures. The mass fractions in this figure are normalized with the maximum value of the mass fraction of the respective species in the unstrained 1D flame.

In case II (deflagration), Fig. 11, the scatter plots of CH_3 and HO_2 mass fractions depict similar trends with those of the 1D unstrained flamelets, which suggests that the initiated fronts in case II have similar thermochemical characteristics with that of the unstrained 1D premixed flames. In case III, however, 1D profiles of the unstrained flamelets and the scatter data portray a significant departure. In particular, the 3D data in case III show that the distribution of both CH_3 and HO_2 are limited to narrow ranges of the progress variable at different time instances. This observation is consistent with the limited distribution of the progress variable in case III, as observed earlier in Fig. 10.

As a closing remark, the theoretical combustion mode diagrams under turbulent conditions are re-evaluated in the following section and a correction factor is proposed to modify the inconsistency between the 3D numerical simulation results and predictions of the theory.

4.4. Correction factor for the turbulent β -curve

While according to the presented β -curve profiles in Fig. 4, the combustion mode in case II was expected to be spontaneous, the presented analyses showed that this case is deflagrative. According to a RANS-based approach by Savard et al. [61], a fitting coefficient in the

order of ≈ 0.1 – 0.2 should be introduced when the turbulence diffusivity is approximated by the product of the turbulence length-scale and velocity. Therefore, we consider a conservative correction factor in our definition of ν_t . We define a corrected turbulence diffusivity as $\nu_t^c = \alpha_c \times l_t \times u_t$ with a correction factor $\alpha_c = 0.2$. The modified version of the combustion mode diagrams at $\beta = 1$, which were presented before in Fig. 4, are shown in Fig. 13 with ν_t^c marked on the profiles for different turbulence velocities in cases I–IV. The modified combustion mode diagrams in Fig. 13 are able to properly capture the identified modes of combustion in cases I–IV from the numerical results. Finally, it should be mentioned that although a large uncertainty exists in the value of α_c , our results show that $\alpha_c \approx 0.1$ – 0.2 is a good approximation for the test cases conducted in this work. However, the uncertainty of α_c parameter might still need further validations in future studies.

5. Conclusions

In this work, effects of (1) hydrogen enrichment and (2) turbulence intensity on the modes of combustion in n -dodecane/methane stratified mixtures were studied and the theoretical combustion mode diagrams were re-validated for new mixtures and against the 3D turbulent data. First, the combustion modes in different DF blends consisting of n -dodecane and different blending ratios of hydrogen enriched methane, under pressure and temperature conditions relevant to RCCI engines and under laminar conditions were investigated. Various levels of the HRF (n -dodecane) stratification in the LRF mixture (methane/hydrogen) in the (λ, Y') space were studied using 1D numerical simulations with detailed chemical kinetics. Three LRF mixtures were considered: methane/hydrogen(%v/v): 100/0(DF-x0), 20/80(DF-x0.8), and 0/100(DF-x1). Second, for a specific point in the (λ, Y') space and for the DF n -dodecane/methane mixture, 3D numerical simulations with detailed chemistry were carried out. The turbulent field was initialized by the Passot–Pouquet turbulent kinetic energy spectrum function at four different turbulence intensity levels (cases I–IV). The following main conclusions were made:

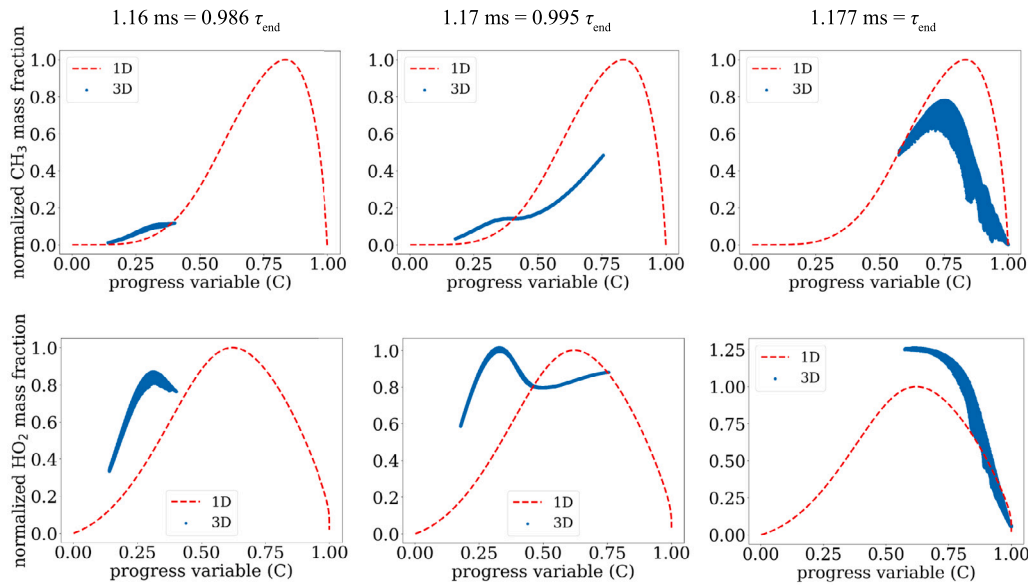


Fig. 12. Scatter data of CH_3 and HO_2 mass fractions in case III superimposed on the profiles of unstrained 1D premixed flames in the progress variable space at different time. In case III, CH_3 and HO_2 are formed within a limited range of the progress variable at each time.

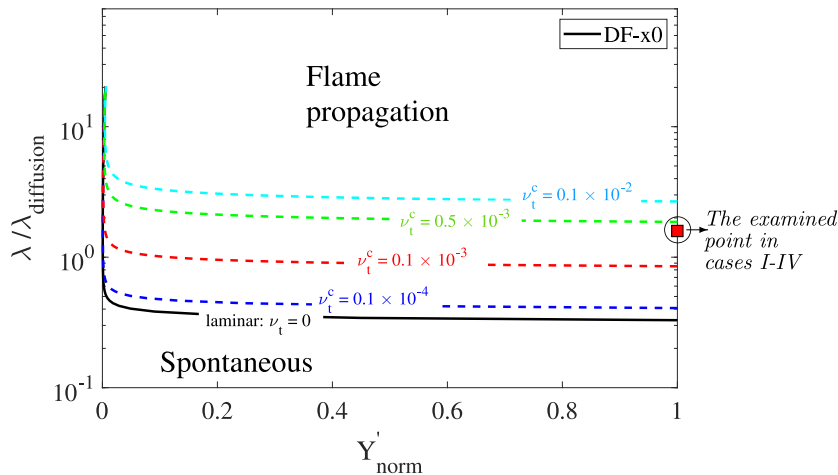


Fig. 13. Corrected combustion mode diagrams with $\alpha_c = 0.2$ for turbulent conditions considered in cases I–IV. Cases I ($\nu_t = 10^{-4}$, $\nu_t^c = 0.2 \times 10^{-4}$ m²/s) and II ($\nu_t = 10^{-3}$, $\nu_t^c = 0.2 \times 10^{-3}$ m²/s) are deflagrative, while cases III ($\nu_t = 5 \times 10^{-3}$, $\nu_t^c = 10^{-3}$ m²/s) and IV ($\nu_t = 10^{-2}$, $\nu_t^c = 0.2 \times 10^{-2}$ m²/s) are spontaneous.

- According to the theory (β -curve) and 1D numerical simulations, hydrogen enrichment of the premixed methane/air mixture can slightly increase the prevalence of the deflagration to spontaneous combustion mode under laminar conditions.
- By adding hydrogen to the premixed methane/air mixture, combustion duration shortens significantly (≈ 9 times shorter in DF-x1 compared to DF-x0).
- Since 3D simulations with hydrogen enrichment are assessed to be computationally super-expensive, turbulent 3D simulations are carried out only for *n*-dodecane/methane mixtures without hydrogen enrichment. However, according to the 1D simulations results, the role of hydrogen enrichment in switching the combustion mode is expected to be of minor importance.
- For the four considered 3D turbulent cases with different turbulence velocities and similar stratification levels, the budget term analysis and the PDF profiles of the progress variable and mixture fraction gradients show that cases I and II with smaller initial

- turbulence velocity are deflagrative, while cases III and IV are spontaneous. In addition, in contrast to the cases which are in the spontaneous regime, the key intermediate species profiles in the deflagrative cases follow those of the 1D unstrained laminar premixed flames in the progress variable space.
- The deflagrative turbulent cases (I and II) present an order of magnitude longer combustion duration compared to the spontaneous cases (III and IV). In addition, right before ignition, the mixture is significantly more homogeneous in cases III and IV (spontaneous) compared to cases I and II (deflagrative).
- With a proposed correction factor for turbulence diffusivity, the β -curve theory presents a reasonable match with the identified modes of combustion in 3D numerical simulations.

As a closing remark, we note that this study attempts to promote using analytical tools, such as the one proposed here, to study the impact of changing fuel combinations on the combustion mode in DF engines,

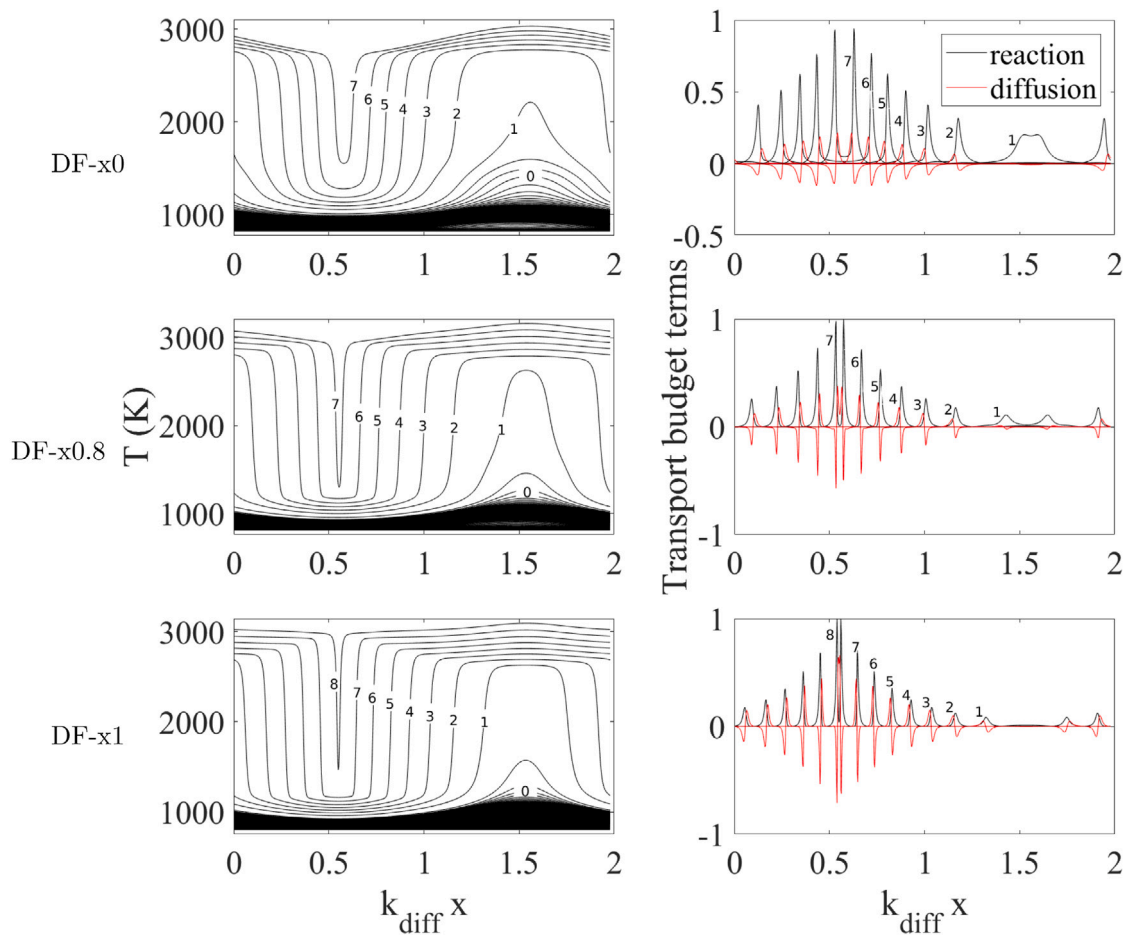


Fig. A.1. Time evolution of the reaction fronts for the selected point in Fig. 2 ($\lambda/\lambda_{diff} = 0.316$ and $Y'_{norm} = 1$) for DF-x0 (upper row), DF-x0.8 (middle row), and DF-x1 (lower row) under laminar conditions and using the unity Lewis model. Numbers represent time intervals of 4, 3, and 2 (μs) for DF-x0, DF-x0.8, and DF-x1, respectively. Number 0 represents a cluster of time-steps corresponding to the ignition kernel formation. (For interpretation of the references to color in this figure legend, the reader is referred to the web version of this article.)

especially when spray and engine numerical simulations are computationally super-expensive and sometimes impossible with the current computational resources. For instance, when hydrogen (which requires advanced diffusion models) is included, detailed numerical simulations under engine-relevant conditions using large chemical mechanisms (to include large hydrocarbons such as diesel) are computationally expensive and infeasible. Therefore, studies like the present work are required to validate the available analytical tools to help in paving the way towards using hydrogen in practical DF combustion systems. As a future research avenue, we intend to validate the proposed analytical tool against the experimental data in DF engines.

Declaration of competing interest

The authors declare that they have no known competing financial interests or personal relationships that could have appeared to influence the work reported in this paper.

Acknowledgments

This study is financially supported by the Academy of Finland (grant numbers 332784 and 318024). We acknowledge CSC (Finnish IT Center for Science) for providing the computational resources.

Appendix A. Effect of diffusion models on 1D results

In this appendix, we briefly evaluate the effect of using the unity Lewis model on the 1D laminar results for DF-x0, DF-x0.8, and DF-x1 compared to the utilized MA model in the paper. Here, the 1D numerical simulations introduced in Section 3.2 are repeated using the unity Lewis model for the 60 1D simulations. We note that, as mentioned in Section 3.2, the choice of the diffusion model does not change the combustion mode in any of the 60 simulation points considered herein. However, there are slight changes in τ_2 and $\delta\tau$ for DF-x0.8 and DF-x1 when results of the two models are compared. It is noteworthy that small fractions of hydrogen in the total mixture (considering its lean condition and the presence of other fuels in the mixture) as well as ignition onset in a short period of time after the start of the simulations are the two main reasons for the mitigation of the effect of hydrogen diffusion on the overall conclusions in this study. Finally, the results of the same simulations in Fig. 3 are presented in Fig. A.1 using the unity Lewis model. It is observed that the difference between the results of the unity Lewis and MA models for DF-x0 is negligible and hard to identify by comparing the two figures. However, hydrogen diffusion affects the profiles in DF-x0.8 and DF-x1. As mentioned earlier, slight changes in τ_2 and $\delta\tau$ are observed. With the unity Lewis model, τ_2 is 0.88, 0.695, and 0.721 ms and $\delta\tau$ is 0.135, 0.02, and 0.016 ms for DF-x0, DF-x0.8, and DF-x1 mixtures in Fig. A.1, respectively.

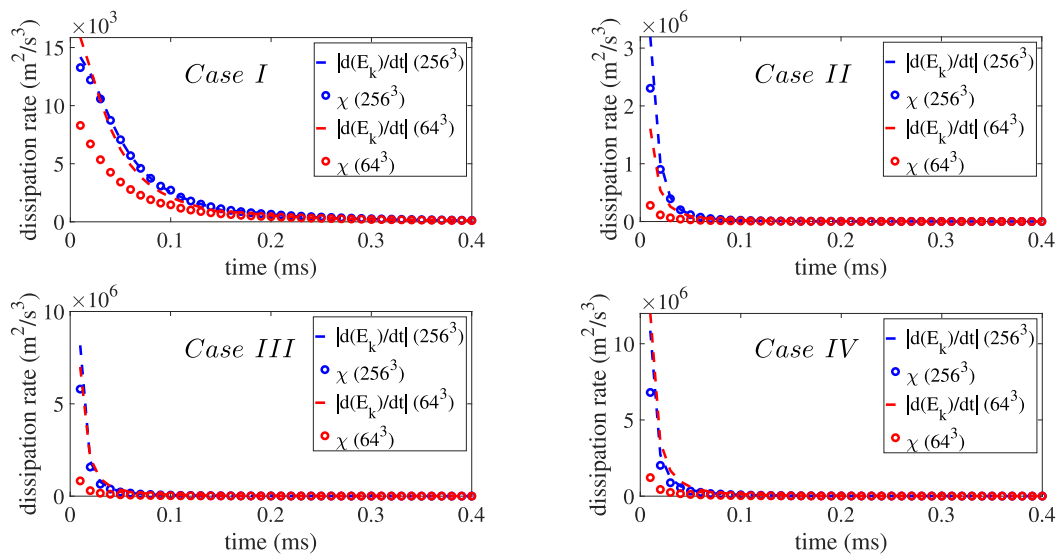


Fig. B.1. Time evolution of the gradient of integrated kinetic energy ($d(E_k)/dt$) and the total rate of viscous dissipation (χ) for cases I–IV with 64^3 and 256^3 cells.

Appendix B. Kinetic energy dissipation in 3D turbulent cases

In this appendix, we evaluate time evolution of the integrated kinetic energy dissipation ($d(E_k)/dt$) against the total rate of viscous dissipation (χ) for the four turbulent cases in Table 3 with two different grid resolutions: 64 and 256 grid points in each direction of the cubic domain. We use non-reacting numerical simulations in this part since the main idea is to assess the effect of grid resolution on energy dissipation. Here, $E_k = \frac{1}{V} \int_V 0.5 u_i^2 dV$ and $\chi = \frac{1}{V} \int_V \nu |\nabla u_i|^2 dV$, where V denotes the volume and u_i is the velocity component in the i direction (x , y , or z). This comparison provides information on the accuracy of the results with different grid points.

The results for the four cases are presented in Fig. B.1. It is observed that higher resolution in all cases leads to more consistency between $d(E_k)/dt$ and χ . In case I, which is resolved with 256^3 cells, $d(E_k)/dt$ and χ lie on top of each other with the 256^3 grid, while the 64^3 grid leads to a significant departure of $d(E_k)/dt$ from χ . In other cases, it is observed that the 256^3 grid does not resolve the initial Kolmogorov length-scale, as expected since the resolution is larger than the initial Kolmogorov length-scale. However, the kinetic energy dissipates quickly after the simulations start and $d(E_k)/dt$ and χ start to match in a short period after the initial time. This observation suggests that only case I is fully-resolved in this study. On the other hand, case II is fairly resolved while cases III and IV are under-resolved. However, since decaying turbulence is used in this work, turbulence length-scales are resolved in cases III and IV at later time-steps in the simulations, when chemical reactions kick in around the first-stage ignition time. We note, however, that the initial departure of $d(E_k)/dt$ from χ may introduce errors in the results of cases III and IV in this study.

References

- [1] Reitz RD, Duraisamy G. Review of high efficiency and clean reactivity controlled compression ignition (RCCI) combustion in internal combustion engines. *Prog Energy Combust Sci* 2015;46(Supplement C):12–71.
- [2] Di Blasio G, Belgiorno G, Beatrice C. Effects on performances, emissions and particle size distributions of a dual fuel (methane-diesel) light-duty engine varying the compression ratio. *Appl Energy* 2017;204:726–40.
- [3] Belgiorno G, Di Blasio G, Beatrice C. Parametric study and optimization of the main engine calibration parameters and compression ratio of a methane-diesel dual fuel engine. *Fuel* 2018;222:821–40.
- [4] Zeldovich Y. Regime classification of an exothermic reaction with nonuniform initial conditions. *Combust Flame* 1980;39(2):211–4.
- [5] Li J, Yang W, Zhou D. Review on the management of RCCI engines. *Renew Sustain Energy Rev* 2017;69(Supplement C):65–79.
- [6] Zhang F, Yu R, Bai XS, Yao M, Peng Z. Direct numerical simulation of flame/spontaneous ignition interaction fueled with hydrogen under SACI engine conditions. *Int J Hydrog Energy* 2017;42(6):3842–52.
- [7] Savard B, Hawkes ER, Aditya K, Wang H, Chen JH. Regimes of premixed turbulent spontaneous ignition and deflagration under gas-turbine reheat combustion conditions. *Combust Flame* 2019;208:402–19.
- [8] Savard B, Wehrfritz A, Lam K, Margerte Q, Ferney L, Farjam S. Decreased mixture reactivity and hot flame speed in the products of diffusion-affected autoignitive cool flames in the NTC regime. *Combust Flame* 2020;222:434–45.
- [9] Badr O, Karim G. Flame propagation in stratified methane-air mixtures. *J Fire Sci* 1984;2(6):415–26.
- [10] Barlow RS, Wang GH, Anselmo-Filho P, Sweeney MS, Hochgreb S. Application of Raman/Rayleigh/LIF diagnostics in turbulent stratified flames. *Proc Combust Inst* 2009;32(1):945–53.
- [11] Seffrin F, Fuest F, Geyer D, Dreizler A. Flow field studies of a new series of turbulent premixed stratified flames. *Combust Flame* 2010;157(2):384–96.
- [12] Butz D, Hartl S, Popp S, Walther S, Barlow RS, Hasse C, Dreizler A, Geyer D. Local flame structure analysis in turbulent CH₄/air flames with multi-regime characteristics. *Combust Flame* 2019;210:426–38.
- [13] Sweeney MS, Hochgreb S, Dunn MJ, Barlow RS. The structure of turbulent stratified and premixed methane/air flames II: Swirling flows. *Combust Flame* 2012;159(9):2912–29.
- [14] Sweeney MS, Hochgreb S, Dunn MJ, Barlow RS. The structure of turbulent stratified and premixed methane/air flames I: Non-swirling flows. *Combust Flame* 2012;159(9):2896–911.
- [15] Pires Da Cruz A, Dean AM, Grenda JM. A numerical study of the laminar flame speed of stratified methane/air flames. *Proc Combust Inst* 2000;28(2):1925–32.
- [16] Sankaran R, Im HG. Dynamic flammability limits of methane/air premixed flames with mixture composition fluctuations. *Proc Combust Inst* 2002;29(1):77–84.
- [17] Richardson E, Granet V, Eyssartier A, Chen J. Effects of equivalence ratio variation on lean, stratified methane–air laminar counterflow flames. *Combust Theory Model* 2010;14:775–92.
- [18] Proch F, Kempf AM. Numerical analysis of the cambridge stratified flame series using artificial thickened flame LES with tabulated premixed flame chemistry. *Combust Flame* 2014;161(10):2627–46.
- [19] Shi X, Chen JY, Chen Z. Numerical study of laminar flame speed of fuel-stratified hydrogen/air flames. *Combust Flame* 2016;163:394–405.
- [20] Turkeri H, Zhao X, Pope SB, Muradoglu M. Large eddy simulation/probability density function simulations of the cambridge turbulent stratified flame series. *Combust Flame* 2019;199:24–45.
- [21] Inanc E, Chakraborty N, Kempf AM. Analysis of mixture stratification effects on unstrained laminar flames. *Combust Flame* 2020;219:339–48.
- [22] Lipatnikov AN. Stratified turbulent flames: Recent advances in understanding the influence of mixture inhomogeneities on premixed combustion and modeling challenges. *Prog Energy Combust Sci* 2017;62:87–132.
- [23] Tomidokoro T, Yokomori T, Ueda T, Im HG. A computational analysis of strained laminar flame propagation in a stratified CH₄/H₂/air mixture. *Proc Combust Inst* 2021;38(2):2543–50.
- [24] Tomidokoro T, Yokomori T, Im HG. Numerical study on propagation and NO reduction behavior of laminar stratified ammonia/air flames. *Combust Flame* 2022;241:112102.

- [25] Chen JH, Hawkes ER, Sankaran R, Mason SD, Im HG. Direct numerical simulation of ignition front propagation in a constant volume with temperature inhomogeneities: I. Fundamental analysis and diagnostics. *Combust Flame* 2006;145(1–2):128–44.
- [26] Pal P, Valorani M, Arias PG, Im HG, Wooldridge MS, Ciottoli PP, Galassi RM. Computational characterization of ignition regimes in a syngas/air mixture with temperature fluctuations. *Proc Combust Inst* 2017;36(3):3705–16.
- [27] Pan J, Wei H, Shu G, Chen Z, Zhao P. The role of low temperature chemistry in combustion mode development under elevated pressures. *Combust Flame* 2016;174:179–93.
- [28] Yoo CS, Lu T, Chen JH, Law CK. Direct numerical simulations of ignition of a lean n-heptane/air mixture with temperature inhomogeneities at constant volume: Parametric study. *Combust Flame* 2011;158(9):1727–41.
- [29] Sankaran R, Im HG, Hawkes ER, Chen JH. The effects of non-uniform temperature distribution on the ignition of a lean homogeneous hydrogen–air mixture. *Proc Combust Inst* 2005;30(1):875–82.
- [30] Hawkes ER, Sankaran R, Pébay PP, Chen JH. Direct numerical simulation of ignition front propagation in a constant volume with temperature inhomogeneities: II. Parametric study. *Combust Flame* 2006;145(1–2):145–59.
- [31] Zhang H, Hawkes ER, Chen JH, Kook S. A numerical study of the autoignition of dimethyl ether with temperature inhomogeneities. *Proc Combust Inst* 2013;34(1):803–12.
- [32] Bansal G, Im HG. Autoignition and front propagation in low temperature combustion engine environments. *Combust Flame* 2011;158(11):2105–12.
- [33] Gupta S, Im HG, Valorani M. Analysis of n-heptane auto-ignition characteristics using computational singular perturbation. *Proc Combust Inst* 2013;34(1):1125–33.
- [34] Bansal G, Mascarenhas A, Chen JH. Direct numerical simulations of autoignition in stratified dimethyl-ether (DME)/air turbulent mixtures. *Combust Flame* 2015;162(3):688–702.
- [35] Im HG, Pal P, Wooldridge MS, Mansfield AB. A regime diagram for autoignition of homogeneous reactant mixtures with turbulent velocity and temperature fluctuations. *Combust Sci Technol* 2015;187(8):1263–75.
- [36] Dai P, Chen Z, Chen S, Ju Y. Numerical experiments on reaction front propagation in n-heptane/air mixture with temperature gradient. *Proc Combust Inst* 2015;35(3):3045–52.
- [37] Pal P, Mansfield AB, Arias PG, Wooldridge MS, Im HG. A computational study of syngas auto-ignition characteristics at high-pressure and low-temperature conditions with thermal inhomogeneities. *Combust Theory Model* 2015;19(5):587–601.
- [38] Luong MB, Hernandez Perez FE, Sow A, Im HG. Prediction of ignition regimes in DME/Air mixtures with temperature and concentration fluctuations. In: *AIAA scitech 2019 forum*. 2019, p. 2241.
- [39] Sun W, Won SH, Gou X, Ju Y. Multi-scale modeling of dynamics and ignition to flame transitions of high pressure stratified n-heptane/toluene mixtures. *Proc Combust Inst* 2015;35(1):1049–56.
- [40] Zhou D, Yang W, An H, Li J, Shu C. A numerical study on RCCI engine fueled by biodiesel/methanol. *Energy Convers Manage* 2015;89:798–807.
- [41] Kahila H, Wehrfritz A, Kaario O, Vuorinen V. Large-eddy simulation of dual-fuel ignition: Diesel spray injection into a lean methane-air mixture. *Combust Flame* 2019;199:131–51.
- [42] Kahila H, Kaario O, Ahmad Z, Ghaderi Masouleh M, Tekgül B, Larmi M, Vuorinen V. A large-eddy simulation study on the influence of diesel pilot spray quantity on methane-air flame initiation. *Combust Flame* 2019;206:506–21.
- [43] Srna A, Bolla M, Wright YM, Herrmann K, Bombach R, Pandurangi SS, Boulouchos K, Bruneaux G. Effect of methane on pilot-fuel auto-ignition in dual-fuel engines. *Proc Combust Inst* 2019;37(4):4741–9.
- [44] Srna A, von Rotz B, Bolla M, Wright YM, Herrmann K, Boulouchos K, Bruneaux G. Experimental investigation of pilot-fuel combustion in dual-fuel engines, Part 2: Understanding the underlying mechanisms by means of optical diagnostics. *Fuel* 2019;255:115766.
- [45] Tekgül B, Kahila H, Kaario O, Vuorinen V. Large-eddy simulation of dual-fuel spray ignition at different ambient temperatures. *Combust Flame* 2020;215:51–65.
- [46] Tekgül B, Kahila H, Karimkashi S, Kaario O, Ahmad Z, Lendormy E, Hyvönen J, Vuorinen V. Large-eddy simulation of spray assisted dual-fuel ignition under reactivity-controlled dynamic conditions. *Fuel* 2021;293:120295.
- [47] Demosthenous E, Borghesi G, Mastorakos E, Cant RS. Direct numerical simulations of premixed methane flame initiation by pilot n-heptane spray autoignition. *Combust Flame* 2016;163:122–37.
- [48] Demosthenous E, Mastorakos E, Stewart Cant R. Direct numerical simulations of dual-fuel non-premixed autoignition. *Combust Sci Technol* 2016;188(4–5):542–55.
- [49] Luong MB, Sankaran R, Yu GH, Chung SH, Yoo CS. On the effect of injection timing on the ignition of lean PRF/air/EGR mixtures under direct dual fuel stratification conditions. *Combust Flame* 2017;183:309–21.
- [50] Luong MB, Yu GH, Chung SH, Yoo CS. Ignition of a lean PRF/air mixture under RCCI/SCCI conditions: A comparative DNS study. *Proc Combust Inst* 2017;36(3):3623–31.
- [51] Luong MB, Yu GH, Chung SH, Yoo CS. Ignition of a lean PRF/air mixture under RCCI/SCCI conditions: Chemical aspects. *Proc Combust Inst* 2017;36(3):3587–96.
- [52] Hu S, Gong C, Bai X-S. Dual fuel combustion of N-heptane/methanol-air-EGR mixtures. *Energy Procedia* 2017;105:4943–8.
- [53] Zhou D, Yang W, Zhao F, Li J. Dual-fuel RCCI engine combustion modeling with detailed chemistry considering flame propagation in partially premixed combustion. *Appl Energy* 2017;203:164–76.
- [54] Yu GH, Luong MB, Chung SH, Yoo CS. Ignition characteristics of a temporally evolving n-heptane jet in an iso-octane/air stream under RCCI combustion-relevant conditions. *Combust Flame* 2019;208:299–312.
- [55] Seddik O, Pandurangi S, Bolla M, Boulouchos K, Srna A, Wright YM. Flamelet generated manifolds applied to dual-fuel combustion of lean methane/air mixtures at engine relevant conditions ignited by n dodecane micro pilot sprays. In: *SAE Tech. Pap. Vol. 2019-April*. 2019.
- [56] Xu S, Zhong S, Hadadpour A, Zhang Y, Pang KM, Jangi M, Fatehi H, Bai XS. Large-eddy simulation of the injection timing effects on the dual-fuel spray flame. *Fuel* 2022;310:122445.
- [57] Schlatter S, Schneider B, Wright YM, Boulouchos K. N-heptane micro pilot assisted methane combustion in a rapid compression expansion machine. *Fuel* 2016;179:339–52.
- [58] Liu H, Tang Q, Yang Z, Ran X, Geng C, Chen B, Feng L, Yao M. A comparative study on partially premixed combustion (PPC) and reactivity controlled compression ignition (RCCI) in an optical engine. *Proc Combust Inst* 2019;37(4):4759–66.
- [59] Karimkashi S, Kahila H, Kaario O, Larmi M, Vuorinen V. A numerical study on combustion mode characterization for locally stratified dual-fuel mixtures. *Combust Flame* 2020;214:121–35.
- [60] Peters N. *Turbulent combustion*. Cambridge: Cambridge Univ. Press; 2000.
- [61] Savard B, Blanquart G. An a priori model for the effective species lewis numbers in premixed turbulent flames. *Combust Flame* 2014;161(6):1547–57.
- [62] Nieman DE, Dempsey AB, Reitz RD. Heavy-duty RCCI operation using natural gas and diesel. *SAE Int J Engines* 2012;5(2):270–85.
- [63] Doosje E, Willems F, Baert R. Experimental demonstration of RCCI in heavy-duty engines using diesel and natural gas. In: *SAE Tech. Pap.*. 2014.
- [64] Walker NR, Wissink ML, DelVescovo DA, Reitz RD. Natural gas for high load dual-fuel reactivity controlled compression ignition in heavy-duty engines. *J Energy Resour Technol* 2015;137(4):42202.
- [65] Ahmad Z, Kaario O, Qiang C, Vuorinen V, Larmi M. A parametric investigation of diesel/methane dual-fuel combustion progression/stages in a heavy-duty optical engine. *Appl Energy* 2019;251:113191.
- [66] Collodi G, Wheeler F. Hydrogen production via steam reforming with CO₂ capture. *Chem Eng Trans* 2010;19:37–42.
- [67] IEA Hydrogen. *Global trends and outlook for hydrogen*. 2017, December.
- [68] White CM, Steeper RR, Lutz AE. The hydrogen-fueled internal combustion engine: a technical review. *Int J Hydrog Energy* 2006;31(10):1292–305.
- [69] Ebrahimi M, Jazayeri SA. Effect of hydrogen addition on RCCI combustion of a heavy duty diesel engine fueled with landfill gas and diesel oil. *Int J Hydrog Energy* 2019;44(14):7607–15.
- [70] Tutak W, Jamrozik A, Grab-Rogaliński K. Effect of natural gas enrichment with hydrogen on combustion process and emission characteristic of a dual fuel diesel engine. *Int J Hydrog Energy* 2020;45(15):9088–97.
- [71] Kannan J, Gadalla M, Tekgül B, Karimkashi S, Kaario O, Vuorinen V. Large-eddy simulation of tri-fuel ignition: diesel spray-assisted ignition of lean hydrogen–methane–air mixtures. *Combust Theory Model* 2021;25(3):1–24.
- [72] Gadalla M, Kannan J, Tekgül B, Karimkashi S, Kaario O, Vuorinen V. Large-eddy simulation of tri-fuel combustion: Diesel spray assisted ignition of methanol-hydrogen blends. *Int J Hydrog Energy* 2021;46(41):21687–703.
- [73] Cheng Q, Ahmad Z, Kaario O, Vuorinen V, Larmi M. Experimental study on tri-fuel combustion using premixed methane-hydrogen mixtures ignited by a diesel pilot. *Int J Hydrog Energy* 2021;46(40):21182–97.
- [74] Cheng Q, Kaario O, Ahmad Z, Vuorinen V, Larmi M. Effect of pilot fuel properties on engine performance and combustion stability in a tri-fuel engine powered by premixed methane-hydrogen and diesel pilot. *Int J Hydrog Energy* 2021;46(75):37469–86.
- [75] Karimkashi S, Kahila H, Kaario O, Larmi M, Vuorinen V. Numerical study on tri-fuel combustion: Ignition properties of hydrogen-enriched methane-diesel and methanol-diesel mixtures. *Int J Hydrog Energy* 2020;45(7):4946–62.
- [76] Haworth DC, Poinot TJ. Numerical simulations of lewis number effects in turbulent premixed flames. *J Fluid Mech* 1992;244:405–36.
- [77] Paret J, Tabeling P. Intermittency in the two-dimensional inverse cascade of energy: Experimental observations. *Phys Fluids* 1998;10(12):3126–36.
- [78] Vuorinen V, Keskinen K. DNSLab: A gateway to turbulent flow simulation in Matlab. *Comput Phys Comm* 2016;203:278–89.
- [79] Hinze JO. Secondary currents in wall turbulence. *Phys Fluids* 1967;10(9):S122–5.
- [80] Mastorakos E, Baritaud T, Poinot T. Numerical simulations of autoignition in turbulent mixing flows. *Combust Flame* 1997;109(1–2):198–223.
- [81] *Engine combustion network*. Livermore, CA: Combustion research facility, Sandia national laboratories; 2019.

- [82] Kannan J, Gadalla M, Tekgül B, Karimkashi S, Kaario O, Vuorinen V. Large eddy simulation of diesel spray-assisted dual-fuel ignition: A comparative study on two n-dodecane mechanisms at different ambient temperatures. *Int J Engine Res* 2020;22(8):2521–32.
- [83] Karimkashi S, Gadalla M, Kannan J, Tekgül B, Kaario O, Vuorinen V. Large-eddy simulation of diesel pilot spray ignition in lean methane-air and methanol-air mixtures at different ambient temperatures. *Int J Engine Res* 2022;146808742110703.
- [84] Tekgül B, Karimkashi S, Kaario O, Kahila H, Lendormy E, Hyvönen J, Vuorinen V. Large-eddy simulation of split injection strategies in RCCI conditions. *Combust Theory Model* 2022.
- [85] Tekgül B, Peltonen P, Kahila H, Kaario O, Vuorinen V. DLBFOam: An open-source dynamic load balancing model for fast reacting flow simulations in OpenFOAM. *Comput Phys Comm* 2021;267:108073.
- [86] Morev I, Tekgül B, Gadalla M, Shahanaghi A, Kannan J, Karimkashi S, Kaario O, Vuorinen V. Fast reactive flow simulations using analytical Jacobian and dynamic load balancing in OpenFOAM. 34, 2022, 021801,
- [87] Zhong S, Zhang F, Jangi M, Bai XS, Yao M, Peng Z. Structure and propagation of n-heptane/air premixed flame in low temperature ignition regime. *Appl Energy* 2020;275:115320.
- [88] Zhang N, Zhang F, Zhong S, Peng Z, Yu J, Liu H, Xu C. Numerical and theoretical investigation of ethanol/air flame instability. 2020;24:1108–29.
- [89] Zhong S, Zhang F, Peng Z, Bai F, Du Q. Roles of CO₂ and H₂O in premixed turbulent oxy-fuel combustion. *Fuel* 2018;234:1044–54.
- [90] Zhong S, Zhang F, Du Q, Peng Z. Characteristics of reactivity controlled combustion with n-heptane low temperature reforming products. *Fuel* 2020;275:117980.
- [91] Rocha RC, Zhong S, Xu L, Bai XS, Costa M, Cai X, Kim H, Brackmann C, Li Z, Aldein M. Structure and laminar flame speed of an ammonia/methane/air premixed flame under varying pressure and equivalence ratio. *Energy Fuels* 2021;35(9):7179–92.
- [92] Frassoldati A, D'Errico G, Lucchini T, Stagni A, Cuoci A, Faravelli T, Onorati A, Ranzi E. Reduced kinetic mechanisms of diesel fuel surrogate for engine CFD simulations. *Combust Flame* 2015;162(10):3991–4007.
- [93] Nguyen-Bui NT, Harribey T, Chassaing P. Modeling of the interaction between a turbulent flow and an ablatable material. In: 28th Congr. int. coun. aeronaut. sci. 2012, ICAS 2012, Vol. 2. 2012, p. 1272–9.
- [94] Saad T, Sutherland JC. Comment on "Diffusion by a random velocity field" [*Phys. Fluids* 13, 22 (1970)]. *Phys Fluids* 2016;28(11):119101.
- [95] Saad T, Cline D, Stoll R, Sutherland JC. Scalable tools for generating synthetic isotropic turbulence with arbitrary spectra. *AIAA J* 2017;55(1):327–31.
- [96] Richards A, Sutherland JC, Saad T. A fast turbulence generator using graphics processing units. In: 2018 fluid dyn. conf. American Institute of Aeronautics and Astronautics Inc, AIAA; 2018.
- [97] Aspden AJ, Day MS, Bell JB. Towards the distributed burning regime in turbulent premixed flames. *J Fluid Mech* 2019;871:1–21.
- [98] Song W, Hernández Pérez FE, Tingas EA, Im HG. Statistics of local and global flame speed and structure for highly turbulent H₂/air premixed flames. *Combust Flame* 2021;232:111523.
- [99] Driscoll JF, Chen JH, Skiba AW, Carter CD, Hawkes ER, Wang H. Premixed flames subjected to extreme turbulence: Some questions and recent answers. *Prog Energy Combust Sci* 2020;76:100802.